

Poly(Lactic Acid)/Poly(Butylene Succinate) Dual-Layer Membranes With Cellulose Nanowhisker for Heavy Metal Ion Separation

Lau K Kian

Universiti Putra Malaysia

Mohammad Jawaid (✉ jawaid@upm.edu.my)

Universiti Putra Malaysia

Mohamed Mahmoud Nasef

Universiti Teknologi Malaysia

Research Article

Keywords: Poly(lactic acid), Poly(butylene succinate), Cellulose nanowhisker, Dual-layer membranes.

Posted Date: June 1st, 2021

DOI: <https://doi.org/10.21203/rs.3.rs-516511/v1>

License:  This work is licensed under a Creative Commons Attribution 4.0 International License.

[Read Full License](#)

Version of Record: A version of this preprint was published at International Journal of Biological Macromolecules on December 1st, 2021. See the published version at

<https://doi.org/10.1016/j.ijbiomac.2021.10.042>.

1 **Poly(lactic acid)/poly(butylene succinate) dual-layer membranes with cellulose**
2 **nanowhisker for heavy metal ion separation**

3
4 **Lau Kia Kian¹, Mohammad Jawaaid^{1*}, Mohamed Mahmoud Nasef²**

5
6 ¹Laboratory of Biocomposite Technology, Institute of Tropical Forestry and Forest Products (INTROP),
7 Universiti Putra Malaysia, 43400 UPM Serdang, Selangor, Malaysia

8 ²Advanced Materials Research Group, Center of Hydrogen Energy, Malaysia-Japan International Institute of
9 Technology (MJIT), Universiti Teknologi Malaysia, Jalan Sultan Yahya Petra, 54100 Kuala Lumpur,
10 Malaysia.

11 *Corresponding author at: Biocomposite Technology Laboratory, INTROP, Universiti Putra
12 Malaysia, 43400 UPM Serdang, Selangor, Malaysia. Tel.: +603-89466960; Fax: +603-86471896

13 *E-mail: jawaaid@upm.edu.my

14
15 **Abstract**

16 In this study, poly(lactic acid) (PLA)/poly(butylene succinate) (PBS) dual-layer membranes filled with cellulose
17 nanowhisker (CNWs), were fabricated by employing an integrated method combining water vapor-induced and
18 crystallization-induced phase inversions. Four membranes (denoted as C-neat, C-I, C-II, and C-III) loaded with
19 CNWs in the range of 0-3 wt% were prepared and characterized using various materials research aspects. The use
20 of CNWs fillers was found to synergize the precipitation of the polymer layers in the integrated water vapor-
21 induced and crystallization-induced method. With morphological examination, the C-III membrane showed
22 prominent and well-laminated two layers structure, evidencing the great precipitating effect of 3 wt% CNWs on
23 the crystallization the polymeric layers. The increase in CNWs loadings was found to improve the membrane
24 porosity ~~with~~, which was accompanied by a decrease in the pore size. The heat resistance of C-neat membrane
25 was enhanced by CNWs loading of 1 wt% (C-I) whereas it decreased with loadings of 2 and 3 wt% (C-II and C-
26 III) due to flaming behaviour of sulphated nanocellulose. Furthermore, The C-III membrane displayed the best
27 mechanical properties ~~in~~ with respect to tensile strength, elongation at break and Young's modulus compared to
28 other membrane samples. For wastewater filtration performance, the continuous operation test showed that C-III
29 membrane exhibited the highest removal efficiency for both Co²⁺ and Ni²⁺ metal ions reaching 83 and 84%,

30 respectively. Thus, it can be concluded that CNWs filled dual-layer membranes have a strong potential for future
31 development for the removal of heavy metal ions from wastewater streams.

32 **Keywords:** Poly(lactic acid); Poly(butylene succinate); Cellulose nanowhisker; Dual-layer membranes.

33

34 **1. Introduction**

35 Membrane technology has been greatly grown for separation and purification applications in various fields
36 including wastewater treatment, hemodialysis, food and beverages and pharmaceutical in past few decades.
37 Particularly, membrane filtration techniques have been widely used in separating various organic and chemical
38 pollutants (Xia et al. 2018). In recent decades, the growing use of chemicals in various industries such as tinnaries,
39 textiles, electronic, automobile and mining resulting in water contamination with heavy metal ions posing serious
40 health issues (human, animal and aquatic life) because of their acute toxicities and carcinogenic nature (Karim et
41 al. 2016). Thus, separation of such heavy metal ions have been one of major separation tasks of various
42 technologies including membrane separation technology (Bolisetty et al. 2019). Moreover, the employment of
43 membrane technology for wastewater filtration is also regarded as an reliable and effective approach to mitigate
44 the crisis of water scarcity (Xia et al. 2018).

45 Polymeric materials are widely used in producing membrane owing to their simple processability and fulfilled
46 characteristics for water filtration. Meanwhile, it has also been receiving the interest from scientists and
47 researchers to work on the fabrication techniques to produce high performance membrane (Galiano et al. 2018).
48 Reportedly, polymeric membranes are fabricated by phase inversion (Minbu et al. 2015; Tanaka et al. 2012),
49 electro-spinning (Pillay et al. 2013), freeze-drying (Cai et al. 2017), and particulate leaching /solvent merging
50 (Gokce et al. 2017; Kiadeh et al. 2017) techniques. Phase inversion is commonly known as a method for
51 fabricating porous membrane structure because of its ability to form a polymer skeleton, in which hierarchically
52 linked to the pores organized from microscale to nanoscale. The fabrication process is induced by the non-solvent,
53 especially like water, which normally utilized in the exchange with solvents for precipitating polymeric
54 components (Perazzo et al. 2015; Zhao et al. 2016).

55 Amongst polymer components, poly(lactic acid) (PLA) is advantageous for membrane fabrication due to its stable
56 crystallization in porosity formation, good thermal tolerance, great mechanical as well as its sustainable and
57 renewable natures (Hamad et al. 2018). Tanaka et al. (2012) had prepared porous poly(L-lactic acid) membranes

58 for microfiltration application by using water induced phase inversion technique. Lately, Minbu et al. (2015)
59 fabricated poly(L-lactic acid) microfiltration membranes using water induced phase inversion with the aid of
60 surfactant, and more recently Chinyerenwa et al. (2018) utilized hot water droplets induced phase inversion to
61 produce porous polylactic acid (PLA) membranes. Besides this, Gao et al. (2015) had studied the pore formation
62 of poly(L-lactic acid) by applying controlled polyethylene oxide additives, and also Phaechamud and Chitrattha
63 (2016) investigated the porous formation of poly(DL-lactic acid) by using various co-solvents.

64 Recently, nano-sized fillers like nanocellulose (Bai et al. 2015; Zhong et al. 2015), zeolites (Fathizadeh et al. 2011;
65 Huang et al. 2013), and carbon nanotubes (Badawi et al. 2014; Choi et al. 2015) have been incorporated into the
66 polymeric membrane structure in order to improve the porosity, thermal properties, mechanical strength, flux
67 permeability, anti-fouling and separation capability (Li et al. 2016). Nanocellulose, a cellulose derivative, is a
68 promising nano-filler for reinforcing polymeric component by attributing to its heat tolerance, high stiffness and
69 inherent nature of environmental friendly characteristics. Also, the large number of reactive functional groups
70 attached on the nanocellulose surface can contribute to the great interaction with polymeric components (Arjmandi
71 et al. 2016; Sung et al. 2017). Zhong et al. (2015) had reported the fabrication of polysulfone/sulfonated
72 polysulfone composite membrane by improving its hydrophilicity and mechanical properties using cellulose
73 nanofibers. Furthermore, nanocrystalline cellulose was incorporated in polysulfone composite by Bai et al. (2015)
74 to produce porous membrane in good connectivity and enhanced mechanical strength. In accordance with
75 literature studies, nanocellulose particles could form percolating networks by agglomeration, which eventually
76 influenced the polymer interfaces and induced large void formation within membrane (Kargarzadeh et al. 2018;
77 Noorani et al. 2007).

78 Dual-layer membrane is a bilayer porous structure comprising of two different polymeric components with distinct
79 properties. Configuration of dual-layer membrane had been regarded as a well-controlled feature to effectively
80 interact with dispersed nanoparticles in both of the top and bottom polymeric layers. The interaction was generally
81 attributing to the localising effect by the preserved intrinsic characteristic in each separated polymer layer (Xia
82 et al. 2018). Meanwhile, the introducing nanoparticles in dual-layer membrane could improve its separation
83 performance in terms of surface hydrophilicity, flux permeability and anti-fouling properties. Li et al. (2006)
84 fabricated a PES/P84 dual-layer membrane with zeolite beta particle added to PES upper layer to enhance
85 permeability and selectivity for O₂/N₂ and CO₂/CH₄ gas separation. Bonyadi et al. (2007) incorporated clay
86 particles in both of the outer and inner layers of a PVDF/PVDF dual-layer membrane to improve the mechanical
87 strength and modified the surface tension of polymer layers for direct contact membrane distillation process.

88 Currently, Zuo et al. (2017) added Al₂O₃ nanoparticles into the inner layer of PVDF/Ultem dual-layer hollow fiber
89 membranes to improve flux performance and mechanical strength for vacuum membrane distillation. Liu et al.
90 (2015) also reported that the reduced pore size and the improved hydrophilicity of CA/PVDF dual-layer
91 membrane was obtained by the increased TiO₂ nanoparticle loading in the outer layer. Therefore, a desirable dual-
92 layer membrane characteristics could be modified through the incorporation of nanoparticles. However, the dual-
93 layer membranes incorporating organic nanofillers such as nanocrystalline cellulose have not been reported in
94 literature.

95 Considering membrane preparation methods, water vapor-induced phase inversion is considerably facile
96 technique to produce porous membranes that involves coagulation of a polymer solution in a vapourized water,
97 and ultimately leads to the polymer precipitation. However, the uncontrolled exchange rate of the water vapour
98 and solvent phases tends to induce a delamination in the dual-layer polymer matrix and causing a degradation in
99 the membrane properties (Kao et al. 2008; Xia et al. 2018). To overcome this problem, an integrated method
100 combining of water vapor-induced and crystallization-induced phase inversions is applied in this study to
101 fabricate a new dual-layer membrane composed of poly(lactic acid) (PLA) and poly(butylene succinate) (PBS)
102 with nanocellulose fillers such as cellulose nanowhisker (CNWs). The nanocellulose filler not only plays a
103 significant role in regulating the polymer phases separation and crystallization but also triggers hydrophilicity and
104 nucleation effects beside serving as a pore-forming agent. This fabrication concept is motivated by the absence of
105 any investigation on the utilisation of nanocellulose fillers to generate PLA/PBS dual-layer polymeric membrane
106 with high performance in removing metal ions. Meanwhile, the fabricated dual-layer membranes undergo various
107 evaluations of their chemical, physical, thermal and mechanical properties with respect to the variation of
108 nanocellulose fillers content. Also, the wastewater filtration performance of the dual-layer membranes was
109 evaluated for separation of heavy metals such as Co²⁺ and Ni²⁺ ions from solutions.

110

111 **2. Experimental**

112 **2.1. Materials and chemicals**

113 PLA pellet (average MW of 75 kg/mol, density of 1.24 g/cm³ and polydispersity of 1.6) and PBS (average MW
114 of 12 kg/mol and density of 1.26 g/cm³), were purchased from PTT Public Co. Ltd. (Bangkok, Thailand). N,N-
115 dimethylformamide (DMF) (≥ 99.8% purity), chloroform (CHCl₃) (≥ 99.5% purity), cobalt (II) chloride
116 hexahydrate (CoCl₂.6H₂O) (≥ 98% trace metal basis), nickel (II) chloride hexahydrate (NiCl₂.6H₂O) (≥ 98% trace

117 metal basis), sulfuric acid (H₂SO₄) (95-98%) and dialysis tube (10 mm average flat width, 2000 MWCO) were
118 purchased from R&M Chemicals. All chemicals were research grade and used as received. Cellulose nanowhisker
119 (CNW), a nanocellulose was produced from roselle microcrystalline cellulose (MCC) according to the treatment
120 condition as described in next section.

121

122 **2.2. Preparation of cellulose nanowhisker (CNW)**

123 The obtained roselle MCC in previously reported work (Kian et al. 2017) was utilized as starting material for
124 CNW preparation. Hydrolysis at temperature of 45°C was conducted to a 2.5 g MCC with 80 ml of (50% w/w)
125 sulfuric acid solution under vigorous mechanical stirring. At the end of acid hydrolysis, the resultant white
126 colloidal suspension was mixed with cold water and centrifuged at 6000 rpm until a pH value close to 3 was
127 reached. Subsequently, the collected white cloudy suspension was subjected to ultrasonication for 15 min with
128 amplitude of 40% at constant 20 kHz frequency and 500 W power output. The suspension was thereafter left for
129 1 h to sediment the undesired macro-size cellulosic component. Afterwards, the suspension was dialyzed with
130 distilled water to reach value of pH 5. Lastly, the supernatant nanocellulose suspension was collected and freeze
131 dried.

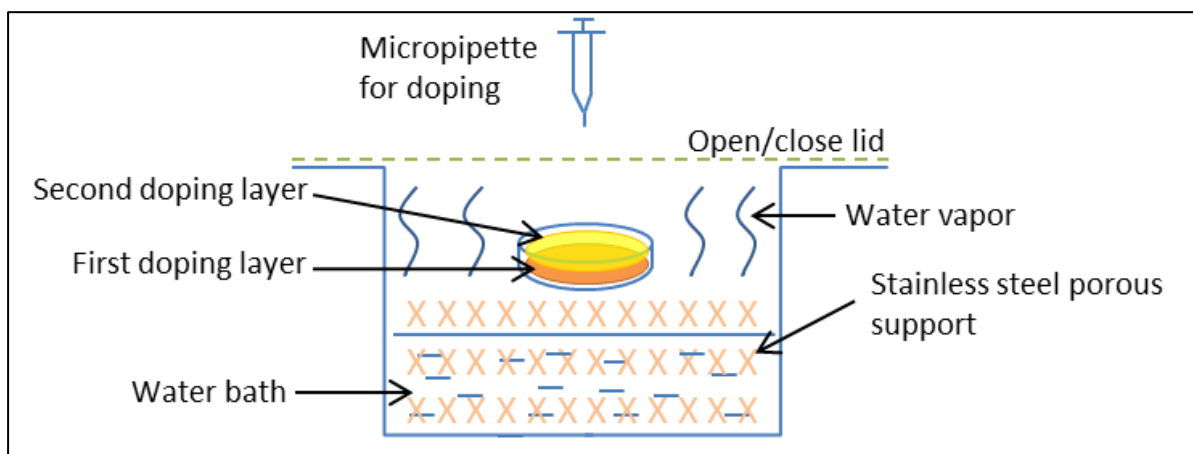
132

133 **2.3. Preparation of dual-layer membranes**

134 A 10 wt% PLA and a 5 wt% PBS solutions were prepared separately by mixing in DMF solvent (on the basis of
135 100 wt%) at 60°C until fully dissolved. Initially, the PLA polymer solution was casted on a petri dish as bottom
136 dope layer and then partially solidified by cooling at room temperature for 5 min. This was followed by casting
137 the second dope solution containing PBS as a top layer on the same petri dish. The petri dish was subsequently
138 placed in a heated bath container filled with water vapor for 5 min to induce the phase inversion for precipitation
139 process as shown in the schematic diagram. A schematic diagram of experimental phase inversion process for
140 dual layer membrane precipitation is presented in Fig. 1. Thereafter, the precipitate-containing solution was
141 subjected to freezing in refrigerator and then gently washed with chloroform to remove the DMF solvent. At the
142 end, a pure PLA/PBS dual-layer membrane was obtained after drying in vacuum oven to remove remained water
143 and solvent traces. For nanocellulose reinforced membranes, a different amounts of nanocellulose were loaded in
144 range of 1-3 wt% during the first mixing step with DMF solvent at 60°C under vigorous stirring. A series of

145 subsequent treatment processes similar to the fabrication of pure PLA/PBS dual-layer membrane were then carried
 146 out. The denotations of obtained dual-layer membranes for pure PLA/PBS and nanocellulose filled PLA/PBS with
 147 their formulation with different loadings are summarized in Table 1.

148



149

150 **Fig. 1.** Schematic diagram of experimental phase inversion process for dual layer membrane precipitation.

151

152 **Table 1.** Denotations of fabricated PLA/PBS dual-layer membranes and their formulation with different
 153 nanocellulose loadings.

Denotations of dual-layer membrane samples	Formulation (on the basis of 100 wt% DMF)		
	PLA (wt%)	PBS (wt%)	Nanocellulose (wt%)
C-neat	10	5	0
C-I	10	5	1
C-II	10	5	2
C-III	10	5	3

154

155 2.4. Nanocellulose characterization

156 The structural morphology of CNW particles was observed with JEOL JEM-2100F transmission electron
 157 microscope (TEM). Preparation of specimens was conducted by negatively staining the CNWs with 2 wt% uranyl
 158 acetate solution prior to deposition on copper grid substrate for drying. Subsequently, the CNW samples undergo
 159 observation with TEM operating at 200 kV accelerating voltage and the obtained data was processed using Image
 160 J software. Furthermore, the Brunauer–Emmett–Teller (BET) analysis was used to determine the specific surface
 161 area of CNWs using a Micromeritics ASAP 2000 instrument, and the samples were degassed by flowing of
 162 nitrogen gas at 60°C for 30 min before analysis.

163 **2.5. PLA/PBS dual-layer membranes characterization**

164 The top surface, bottom surface, and cross section morphology of dual-layer membranes were investigated by a
165 field emission electron microscope (FESEM) under an accelerating voltage in the range of 10-20 kV. Before
166 FESEM observation, the membranes were coated with platinum via sputtering to avoid charging effect. For cross-
167 sectional analysis, the membranes were fractured after dipping in liquid nitrogen prior to gold coating and
168 mounting on sample holders. In addition, the thickness of produced dual-layer membranes was measured with a
169 YASUDA digital film thickness gauge. BET analysis was employed to determine the membrane porosity and
170 average pore size using a Micromeritics ASAP 2000 instrument after degassing in the flow of nitrogen gas at
171 60°C for 30 min prior to analysis. The compositional structure of the membrane samples was examined with
172 Perkin Elmer 1600 Infrared spectrometer (FTIR) within 500–4000 cm⁻¹ wavenumber range. The changes in the
173 crystallinity of the membranes samples was monitored with a SHIMADZU XRD-6000 X-ray diffractometer (XRD)
174 with scanning speed from 5° to 60° at 2 °C/min stepwise and a TA Instruments Q20 differential scanning
175 calorimeter (DSC) with a temperature scanning range from 25°C to 200°C at 5°C min⁻¹ heating rate under nitrogen
176 atmosphere. The collected data from DSC was used to calculate the crystallinity degree of PLA and PBS as below
177 Eq. (1) and Eq. (2), respectively.

178
$$X_c \text{ of PLA} = \frac{\Delta H_m}{93.6} \times 100\% \quad (1)$$

179
$$X_c \text{ of PBS} = \frac{\Delta H_m}{100.7} \times 100\% \quad (2)$$

180 where, ΔH_m is the melting enthalpy of respective polymer.

181 Apart from that, the thermal stability of the samples was investigated with TA Instruments Q500
182 thermogravimetric analyzer (TGA) in a temperature range of 25-1000°C at 20°C/min heating rate. An Instron
183 4400 Universal Tester was used to study the mechanical properties with respect to tensile strength and elongation
184 at break of the samples according to the ASTM D882-12 under a fixed 12.5 mm/min crosshead speed. Also, the
185 wettability of the membrane surface was studied with a KRUSS DSA-100 goniometer and the contact angle was
186 determined after a 2.5 μ L water dropping for 2 seconds.

187

188

189

190 2.6. Performance of dual-layer membranes

191 To evaluate the wastewater filtration performance, model solutions of Co^{2+} and Ni^{2+} were used. Particularly, 50
192 mg/L solutions containing Co^{2+} and Ni^{2+} were prepared separately and used as a stock for all batch and continuous
193 adsorption experiments through a 0.4 g/L solid membrane. In batch adsorption mode, each membrane was
194 incubated in a 100 mL volume of metal ion solution for 180 min. Meanwhile, the removal efficiency (R_e) for metal
195 ions was calculated with the following Eq. (3).

$$196 \quad R_e(\%) = 1 - \frac{C_p}{C_f} \times 100 \quad (3)$$

197 where, C_p and C_f are the metal ion concentrations of permeate and feed solutions respectively, which determined
198 with inductively coupled plasma optical emission spectrometry (ICP-OES). Also, the adsorbed capacity (Q_e) for
199 metal ions was calculated using the Eq. (4).

$$200 \quad Q_e(\text{mg/g}) = \frac{(R_e \times C_f)}{m} \quad (4)$$

201 where, m is the effective mass of membrane subjected to adsorption in metal ion solutions.

202 For continuous adsorption mode, a 100 mL volume of metal ion solution was allowed to flow through a dead-end
203 filtration cell for 180 min under 0.1 MPa applied pressure with a membrane having an effective area of 16 cm².
204 Similarly, the removal efficiency and adsorbed capacity of metal ions were determined using the Eq. (3) and Eq.
205 (4), respectively. Additionally, the flux of pure water and metal ion solution (J) was measured at each 30 min time
206 interval following the Eq. (5).

$$207 \quad J = \frac{V}{A \times t} \quad (5)$$

208 where, V is the volume of pure water or metal ion solution (L), A is the effective area of membrane (m²), and t is
209 the filtration time. Anti-fouling testing was also carried out on the best optimized membrane by second filtration
210 cycle to determine the reversible fouling (R_r), irreversible fouling (R_{ir}), total fouling ratio (R_t), flux recovery of
211 pure water (FR_w) and metal ion solution (FR_p), using Eq. (6), Eq. (7), Eq. (8), Eq. (9), and Eq. (10), respectively.

$$212 \quad R_r = \frac{J_{w2} - J_{p1}}{J_{w1}} \times 100\% \quad (6)$$

213
$$R_{ir} = \frac{J_{w1} - J_{w2}}{J_{w1}} \times 100\% \quad (7)$$

214
$$R_t = 1 - \frac{J_{p1}}{J_{w1}} \times 100\% \quad (8)$$

215
$$FR_w = \frac{J_{w2}}{J_{w1}} \times 100\% \quad (9)$$

216
$$FR_p = \frac{J_{p2}}{J_{p1}} \times 100\% \quad (10)$$

217 where, J_{w1} is the pure water flux, J_{w2} is the water flux of cleaned membrane, J_{p1} is the metal ion solution flux, and
218 J_{p2} is the metal ion solution flux of the cleaned membrane.

219

220 **2.7. Statistical analysis**

221 The BET, mechanical test, and water contact angle data (means, $M \pm$ standard deviation, SD) were obtained with
222 replicates for each membrane sample to provide reproducibility proof in each characterization section of
223 morphology, mechanical and filtration performance, respectively. Statistical comparisons were analysed by using
224 ANOVA (t -test) and the differences with $p \leq 0.05$ (95% confidence level) were considered statistically significant.

225

226 **3. Results and discussion**

227 **3.1. Morphology of nanocelulose and PLA/PBS dual-layer membranes**

228 The CNWs was proved to have a rod-like shape as illustrated TEM image shown in Fig. 2. The measured average
229 size for the CNW rods was in 119.4 ± 0.2 nm length, 18.1 ± 0.5 nm diameter and with aspect ratio of 6.6 ± 0.4 .
230 Meanwhile, the examined specific surface area by BET analysis was 19.32 ± 0.04 m²/g for the cellulose
231 nanowhiskers (CNWs).

232

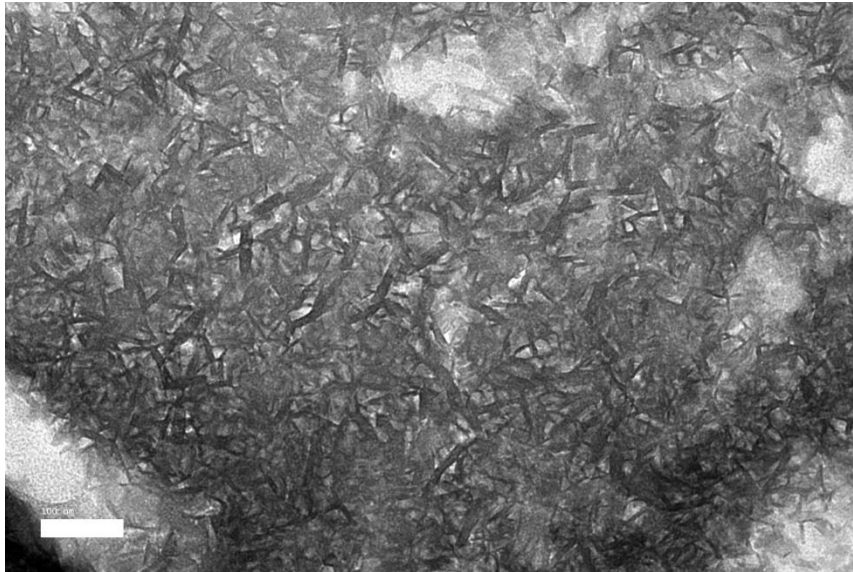


Fig. 2. TEM image of formed CNW.

233

234

235

236 Fig. 3 shows the FESEM images of C-neat, C-I, C-II and C-III membranes. All membrane samples revealed dense
237 top surface (Fig. 3a-d) and porous bottom surface (Fig. 3i-l), which rendered by water vapor-induced phase
238 inversion fabrication (Kao et al. 2008). The propagating circular lines could be observed on the top surfaces for
239 C-I (Fig. 3b), C-II (Fig. 3c) and C-III (Fig. 3d) membranes when compared to the apparently orderless surface of
240 C-neat membrane (Fig. 3a). This implies that the PBS polymer chains were greatly sealed in the membranes by
241 the incorporation of CNWs (Huang et al. 2018). Under magnified viewing, the surface morphology was found to
242 be smoother for C-I (Fig. 3f) as compared with C-neat membrane (Fig. 3e), confirming the improved interaction
243 between polymer chains after the addition of CNWs. With the increased CNWs loadings beyond 1 wt%, rougher
244 surfaces were observed for C-II (Fig. 3g) and C-III (Fig. 3h) membranes. This trend may be attributed to the
245 induced steric hindrance caused by the considerable amount of CNW that resulted in the formation of bulky
246 polymer chains (Bahremand et al. 2017; Zhang and Wang, 2018). Each nanocomposite membrane exhibited well-
247 distributed CNWs on their top surface, and this could endow them with a good initial contacting surface area for
248 adsorbing heavy metal ions in wastewater treatment (Arjmandi et al. 2016; Karim et al. 2016). As viewed from
249 bottom-surface images, C-neat (Fig. 3i) presented apparently tough structure with dented surface. A tremendously
250 change of dented features were observed for C-I (Fig. 3j) and C-II (Fig. 3k) membranes, possibly owing to the
251 unstable exchange rate that occurred between DMF and water vapor for polymer crystallization (Phaechamud and
252 Chitrattha, 2016). However, the addition of 3 wt% CNWs gave a better morphology for C-III (Fig. 3l) membrane,
253 when comparing to C-I and C-II. This was probably ascribed to the homogeneously distribution of CNWs within

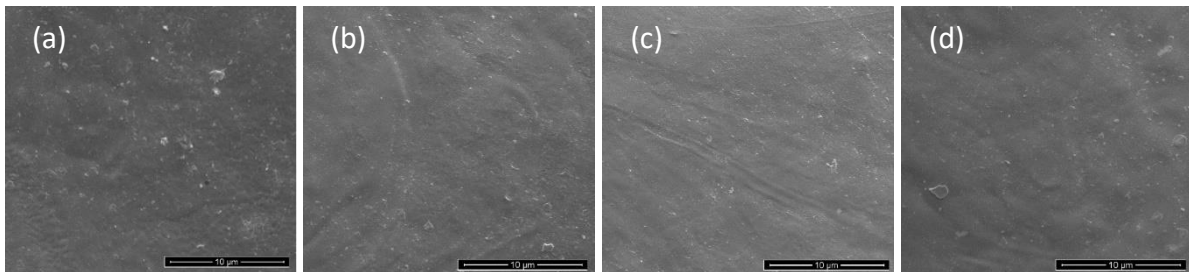
254 C-III membrane, which led to the uniform solid-liquid phase separation (Daraei et al. 2016; Xiong et al. 2017).
255 Furthermore, the incorporation of CNWs contributed to the formation of small cell-like pore features for C-I, C-
256 II and C-III membranes (Fig. 3n-p), as compared to the C-neat membrane (Fig. 3m), which displayed little porous
257 feature and this is because the CNW particles acted as a nucleating agent for promoting cell-sized porous surface.
258 During the crystallization process, small crystals domains were initially formed, and these small crystals
259 subsequently grew into bigger crystals to induce pore formation as a result of coalescence occurred in the later
260 stage (Lin et al. 2015; Wang et al. 2017).

261 Besides, the membrane thickness determined in this work was found in the range of 11 to 13 μm , which speculated
262 that it did not pose significant flux deviation during filtration process. From Table 2 depicting BET data, the
263 porosity was gradually improved from $43 \pm 0.036\%$ for C-neat to $67 \pm 0.024\%$ for C-I membrane, and then further
264 increased to $71 \pm 0.053\%$ and $74 \pm 0.028\%$ for C-II and C-III membranes, respectively. Meanwhile, the average
265 pore sizes were found decreasing from C-neat ($2.45 \pm 0.019 \mu\text{m}$) membrane to C-I ($1.13 \pm 0.017 \mu\text{m}$), C-II (0.86
266 $\pm 0.024 \mu\text{m}$), and C-III ($0.54 \pm 0.015 \mu\text{m}$) following the addition of CNWs (Table 2). This is most likely due to
267 the increase of CNWs amount, which triggered the generation of larger number of small growing crystals domains.
268 Herein, higher porosity was obtained, owing to the greater coalescence effect between the grown crystals.
269 However, due to the saturation state achieved between the CNWs and polymers, the growth of small crystals was
270 suppressed and hence a reduction in the pore size took place with the increase in CNW loadings in the membranes
271 (Mi et al. 2014; Wang et al. 2017). In cross-sectional viewing for C-neat membrane (Fig. 3q), the PLA polymer
272 (bottom thick layer) was layered with PBS polymer (top thin layer). Meanwhile, the top PBS layer was observed
273 extending downwards to the bottom PLA layer, implying the presence of good interfacial adhesion between these
274 two polymers (Liu et al. 2015). On the other hand, the C-I membrane (Fig. 3r) showed leaf-like porous structure,
275 but the distinctly two layers were not likely observed in the membrane. This was probably attributed to the
276 simultaneously increasing free-volume in both PLA and PBS polymers by mixing with 1 wt% CNWs, which
277 greatly enhanced both polymers miscibility (Li et al. 2018; Luzi et al. 2016). When 2 wt% CNW fillers were
278 introduced, the finger-like pore feature began to emerge in C-II membrane (Fig. 3s), and this feature transition
279 implies that an enhancement in polymer rigidity occurred. For C-III (Fig. 3t), a prominent finger shaped porous
280 structure was observed when 3 wt% CNW fillers were incorporated into the membrane, signifying the presence of
281 stable crystallized dual-layer polymer structure (Borkotoky et al. 2018; Liu et al. 2015). The C-III membrane
282 revealed much significant layers of both PLA and PBS than that of C-II. Moreover, the PLA layer formed an
283 interlocking structure with PBS layer for the C-III membrane via the hydrogen bonding interaction generated by

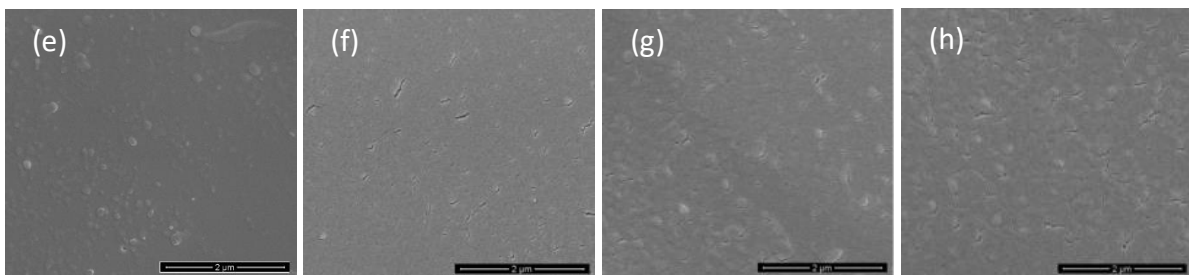
284 the adjacent hydroxyl groups in each polymer layer (Li et al. 2018; Kao et al. 2008). Thus, it can be predict that
285 the lamination between the two layers was stronger in C-III compared to the C-neat membrane and other CNWs
286 reinforced membranes.

287

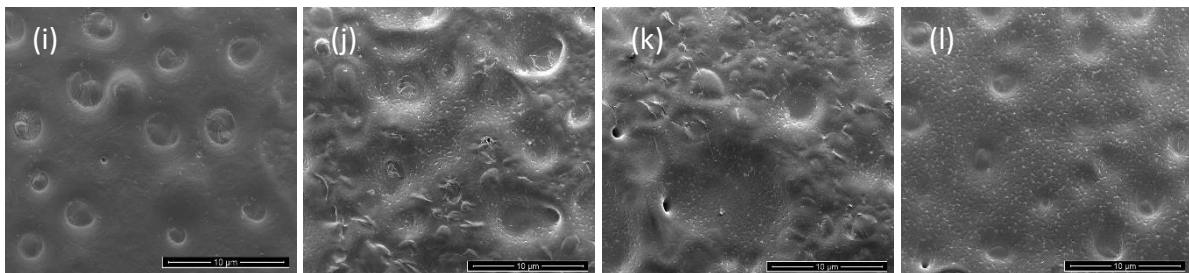
288



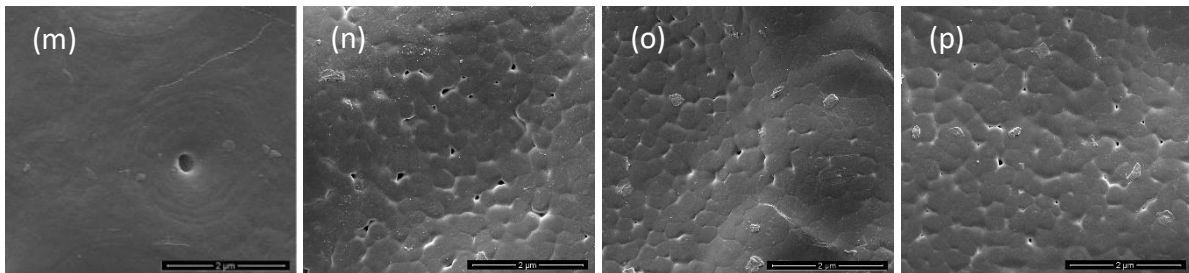
289



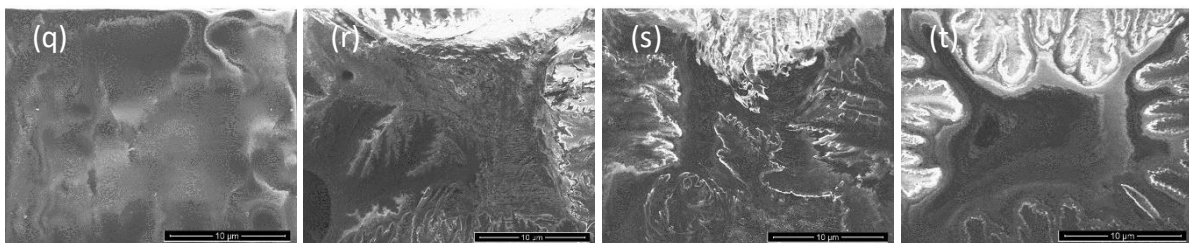
290



291



292



293 **Fig. 3.** FESEM images of C-neat (a, e, i, m, q), C-I (b, f, j, n, r), C-II (c, g, k, o, s), and C-III (d, h, l, p, t) membranes
294 for top-surface at 10000 x (a-d) and 50000 x (e-h) magnifications; bottom-surface at 10000 x (i-l) and 50000 x
295 (m-p) magnifications; cross-sectional view at 10000 x (q-t) magnification morphology.

296

297 **Table 2.** BET data for porosity and average pore size of membranes

Membranes	Porosity (%)	Average pore size (μm)
C-neat	43 ± 0.04^a	2.45 ± 0.02^a
C-I	67 ± 0.02^b	1.13 ± 0.02^b
C-II	71 ± 0.05^c	0.86 ± 0.02^c
C-III	74 ± 0.03^d	0.54 ± 0.01^d

298 ^{a-d}Values within the same column with various superscripts indicate significant differences ($p \leq 0.05$).

299

300 3.2. Physicochemical property

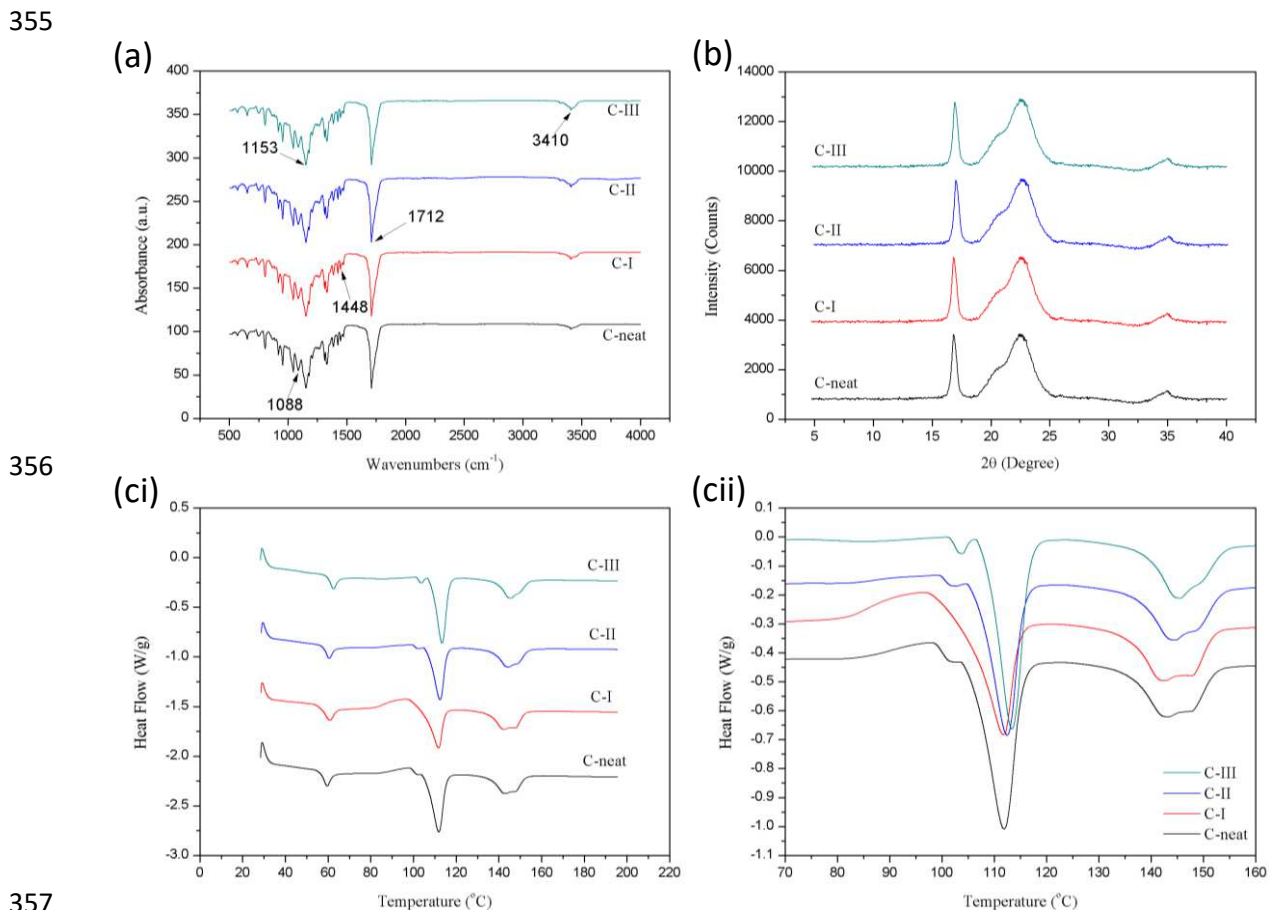
301 The changes in chemical structure were monitored with FTIR and the spectra of the investigated membranes are
 302 shown in Fig. 4a. From Fig. 4a, the nanocellulose filled membranes showed closely similar FTIR spectra with
 303 DL-neat membrane in the region of $500\text{-}2000\text{ cm}^{-1}$. For instance, significant absorbance peaks were observed for
 304 each membrane sample at 1088 cm^{-1} (C-OH bending), 1153 cm^{-1} (C-O-C stretching), 1448 cm^{-1} (CH_3 stretching)
 305 and 1712 cm^{-1} (C=O vibration), which signifies the typical characteristics of the membranes polymer molecules
 306 (Hossain et al. 2014; Huang et al. 2018). Noticeably, the peak at around 3410 cm^{-1} absorbance became sharper
 307 after the addition of nanocellulose to dual-layer membranes and this resembles the cellulose hydroxyl groups (O-
 308 H vibrational stretching) indicating the achievement of good physically mixing of nanocellulose within polymeric
 309 components (Arjmandi et al. 2016; Planellas et al. 2014). Moreover, the absence of new absorbance peak from
 310 the FTIR spectra had proved that no chemical reaction occurred in all nanocellulose filled membranes.

311 XRD diffractograms of the membranes is presented in Fig. 4b. According to literature, the PLA has main
 312 diffraction peaks at $2\Theta = 16.7^\circ(200)$, $19.2^\circ(203)$, and $22.3^\circ(110)$ representing α -form of PDLA or PLLA crystals
 313 with pseudo-orthorhombic system, whereas, PBS showed main diffraction peaks at about $2\Theta = 19.6^\circ(002)$,
 314 $21.8^\circ(012)$, and $22.7^\circ(110)$ resembling α -form with monoclinic system (Planellas et al. 2014; Stoyanova et al.
 315 2014). According to Fig. 4b, predominant peaks at around 16.8° , 20.4° , and 22.5° can be clearly seen in all
 316 membrane samples. Meanwhile, a broad peak was observed for each sample extending from 19° to 26° that
 317 comprised the 20.4° sharp peak and a 22.5° shoulder peak. This results might be contributed by the overlapping
 318 of the crystalline peaks of both PLA and PBS components in the membrane where the adhered interactions
 319 between the two polymeric layers were concieved (Stoyanova et al. 2014). However, the presence of broadly vast
 320 peaks might cover the undetermined regions in this XRD diffractogram representing the level of the adherence
 321 between the two polymeric layers is unvalid. Moreover, distinct peak at 16.8° originated from PLA polymer

322 having similar intensity in all membranes. This showcased the well-define crystalline characteristics for the PLA
323 component existing in all the dual-layer membrane samples (Planellas et al. 2014; Mizuno et al. 2015). A slight
324 peak left shifting could be observed for C-I with 16.7° peak as compared to C-neat with 16.8° peak, revealing the
325 unorder crystal arrangement in the C-I membrane. Nonetheless, the C-II and C-III exhibited their peaks with 17.0°
326 and 17.1° respectively in right shifting to the C-neat, which correlated with the improved crystal lattice
327 organizations (Borkotoky et al. 2018; Chinyerenwa et al. 2018).

328 DSC curves of the fabricated membrane samples and their corrsponding thermal properties data obtained only
329 from first heating runs are presented in Fig. 4c and Table 3, respectively. The glass transition temperature (T_g) of
330 PLA was mildly enhanced for C-I, C-II and C-III membranes when compared to the C-neat, signalling the
331 integration of nanocellulose filler in PLA could reduce its polymeric chain mobility (Fig. 4ci) (Ojijo et al. 2012).
332 Beyond 80°C temperature (Fig. 4cii), the C-neat membrane revealed its exothermic peak at 98.1°C (T_c of PLA)
333 accompanied by a second small exothermic peak at 101.7°C (T_c of PBS). Interestingly, the small secondary
334 exotherm, was not observed in C-I membrane, which rather had been overlapped by the broadly large exothermic
335 peak at 111.9°C. This was likely showing that the distinct crystallization behaviour of both PLA and PBS
336 polymers had somehow collapsed upon loading 1 wt% nanocellulose and subsequently contributed to the C-I
337 membrane with assimilated structure (Haafiz et al. 2015; Zuo et al. 2017). Furthermore, the second observed
338 exotherms in C-II and C-III implied the reformation of dual polymeric membrane structures, which were in line
339 with the discussion in morphological FESEM section. It could be ascribed to the faster growth of PLA and PBS
340 crystals that were promoted by the great nucleating effect of nanoparticles at the 2 and 3 wt% nanocellulose
341 loadings (Planellas et al. 2014; Zhang and Wang, 2018). Furthermore, the PLA and PBS melting temperatures
342 (T_m) (Table 3) were slightly decreased for C-I membrane compared to C-neat, possibly owing to the immiscibility
343 between polymers and nanocellulose to some extents. Meanwhile, the melting temperatures had increased for C-
344 II and C-III membranes. This was attributed to the great localization effect of CNWs in the dual-layer structure
345 of the membrane leading to the better nanocellulose dispersion and adhesion in each polymer layer (Peng et al.
346 2012; Tijink et al. 2012). In addition, both melting peaks became sharper and narrower from C-I to C-III
347 membranes, showing that the increase in filling of nanocellulose could improve the polymer integrity (Xiong et
348 al. 2017). The melting enthalpy (ΔH_m) for both PLA and PBS components was recorded the highest value for C-
349 III membrane. This trend might be imparted by the strong interfaces between CNWs and polymers as well as the
350 strong adherence between the two polymeric layers via hydrogen bonding interaction (Chinyerenwa et al. 2018;
351 Sung et al. 2017). Also, the estimated degress of crystallinity (X_c) for both PLA and PBS polymers was increased

352 from C-neat to C-III membranes (Table 3). Therefore, this confirms that the increment of nanocellulose loadings
 353 enhance the crystallinity of the dual-layer polymeric membrane structure and improve the components adherence
 354 and interfacial resistance.



357
 358 **Fig. 4.** Various changes in properties of dual-layer membranes observed in: (a) FTIR spectra (b) XRD
 359 diffractograms and (ci and cii) full and zoomed DSC curves, respectively.

360

361 **Table 3.** DSC analysis data of membrane samples

Membranes	PLA					PBS			
	T_g (°C) ^a	T_c (°C) ^b	T_m (°C) ^c	ΔH_m (J/g) ^d	X_c (%) ^e	T_c (°C) ^b	T_m (°C) ^c	ΔH_m (J/g) ^d	X_c (%) ^e
C-neat	60.1	98.1	143.2	32.7	34.9	101.7	112.0	17.1	17.0
C-I	60.9	96.9	142.6	33.8	36.1	-	111.9	19.0	18.9
C-II	60.7	99.4	144.5	34.1	36.4	104.6	112.5	20.3	20.2
C-III	62.6	101.3	145.4	35.2	37.6	106.2	113.4	21.4	21.3

362 ^aglass transition temperature, ^bcrystallization temperature, ^cmelting temperature, ^dmelting enthalpy and ^edegree of
 363 crystallinity.

364

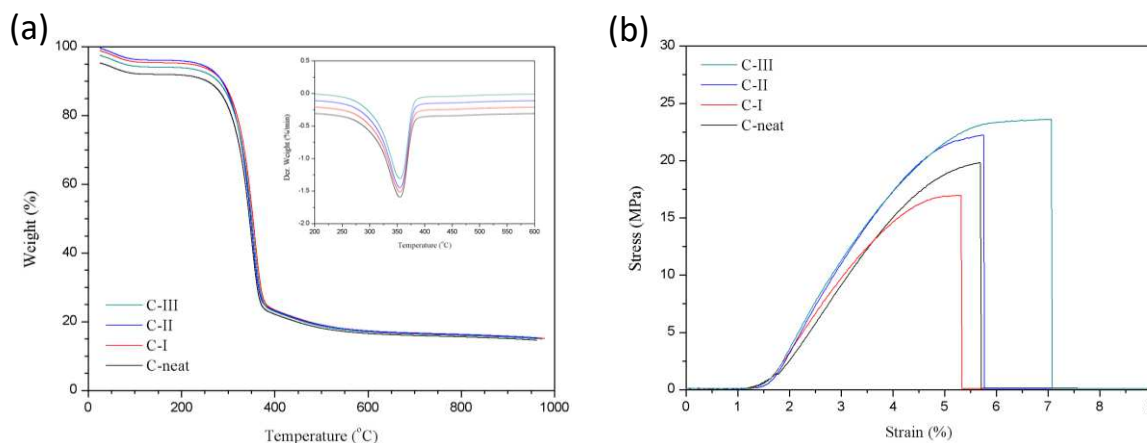
365

366

367 3.3. Thermal stability, mechanical strength, and surface wettability analysis

368 Thermogravimetric and tensile analyses were employed to investigate the applicability of fabricated membranes
369 in harsh conditions. From TGA curve in Fig. 5a, each membrane lost their initial weight in 50-160°C temperature
370 range due to the dehydration of absorbed water moisture from hydrophilic CNWs (Ojijo et al. 2012; Phaechamud
371 and Chitrattha, 2016). Beyond 200°C temperature, those nano-filled membranes presented higher onset
372 degradation temperature (T_{onset}) compared to the C-neat membrane. This indicates that the incorporation of CNWs
373 tends to promote the thermal resistant of both polymer components via the hydroxyl groups interaction (Luzi et
374 al. 2016; Qian and Sheng, 2017). Regarding to the CNWs loadings effect, the onset degradation temperatures
375 were slightly decreased from C-I to C-II membranes, whereas, gradually reduced for the membranes from C-II to
376 C-III (Table 4). This was probably due to the presence of ester sulfate groups on nanocellulose surface, which
377 could initiate the earlier thermal degradation of polymer molecules. Furthermore, the sign of low residue
378 formation ($W_{residue}$) in responding to the high weight loss (W_{loss}) was observed in all membrane samples (Table 4).
379 The C-III membrane revealed significantly high weight residue owing to the flame retardant of crystalline
380 nanocellulose (Luzi et al. 2016; Sung et al. 2017). Additionally, from DTG curve, the C-I membrane had the
381 greatest thermal stability between those membranes with its degradation peak temperature (T_{peak}) at 355.8°C.

382



383

384 **Fig. 5.** (a) TGA curves (with plotted DTG curves) and (b) mechanical stress-strain curves of dual-layer membranes.

385

386

387

388

389

390 **Table 4.** TGA analysis data of membrane samples.

Membranes	T _{onset} (°C) ^a	T _{peak} (°C) ^b	W _{loss} (%) ^c	W _{residue} (%) ^d
C-neat	315.8	354.6	89.4	5.4
C-I	326.8	355.8	89.1	5.6
C-II	324.7	355.3	88.5	6.1
C-III	317.2	355.0	87.9	6.4

391 ^aOnset degradation temperature, ^bdegradation peak temperature, ^cweight loss and ^dchar residual weight.

392

393 For mechanical test (Fig. 5b), both tensile strength and elongation at break were improved for C-II and C-III
 394 membranes when compared with C-neat membrane. However, the C-I membrane presented lower elongation at
 395 break and tensile strength than the other membrane samples. This was possibly attributed to the distinct two
 396 polymeric layers structures in C-neat, C-II and C-III membranes imparting them with better stress transfer
 397 property (Tanaka et al. 2012; Tijink et al. 2012). As for C-I membrane, its collapsed layeric structure resulted in
 398 the PBS upper layer unlikely to reduce stress-strain forces delivered to the PLA bottom layer. Additionally, the
 399 increment of nanocellulose from 2 to 3 wt% tremendously enhanced the elongation at break for C-III membrane
 400 besides the improvement of tensile strength. This was probably resulted from the combined effect of good layers
 401 interfacial adherence and small average pore size in C-III membrane allowing great stress transfer between
 402 nanocellulose and polymers (Gao et al. 2015; Zuo et al. 2017). Also, the Young's modulus measured for
 403 membranes filled with CNWs was consistent with the improvement of the tensile strength (Table 5). The C-III
 404 membrane gave the highest value of Young's modulus with 0.75 ± 0.04 GPa, whereas the C-I membrane displayed
 405 the lowest value of 0.66 ± 0.04 GPa. Hence, from mechanical test results, C-III membrane was regarded having
 406 the balanced elasticity, stiffness, and rigidity for withstanding water flux pressure in filtration process.

407 Apart from that, membranes surface wettability were evaluated by water contact angle as summarized in Table 6.
 408 A contact angle of ($69.2 \pm 0.08^\circ$ at top-surface and $70.4 \pm 0.05^\circ$ at bottom surface) was observed in C-neat
 409 membrane reflecting the PBS top and PLA bottom layers possessed relatively great water-favoured characteristics
 410 probably promoted by their rough surface feature that formed during phase inversion process. Nonetheless, those
 411 nanocellulose filled membranes showed decreased contact angles, indicating the enhanced hydrophilicity on the
 412 membrane surfaces (Xiong et al. 2017).

413

414

415

416

417 **Table 5.** Tensile properties data of membrane samples

Membranes	Tensile strength (MPa)	Elongation at break (%)	Young's modulus (GPa)
C-neat	19.7 ± 0.15 ^a	5.7 ± 0.08 ^a	0.67 ± 0.05 ^a
C-I	16.9 ± 0.14 ^b	5.3 ± 0.06 ^b	0.66 ± 0.04 ^a
C-II	22.1 ± 0.15 ^c	5.8 ± 0.11 ^c	0.73 ± 0.06 ^b
C-III	23.5 ± 0.12 ^d	7.1 ± 0.09 ^d	0.75 ± 0.04 ^b

418 ^{a-d}Values within the same column with various superscripts indicate significant differences ($p \leq 0.05$).

419

420 **Table 6.** Water contact angle of dual-layer membranes with 0-3 wt% CNWs loadings

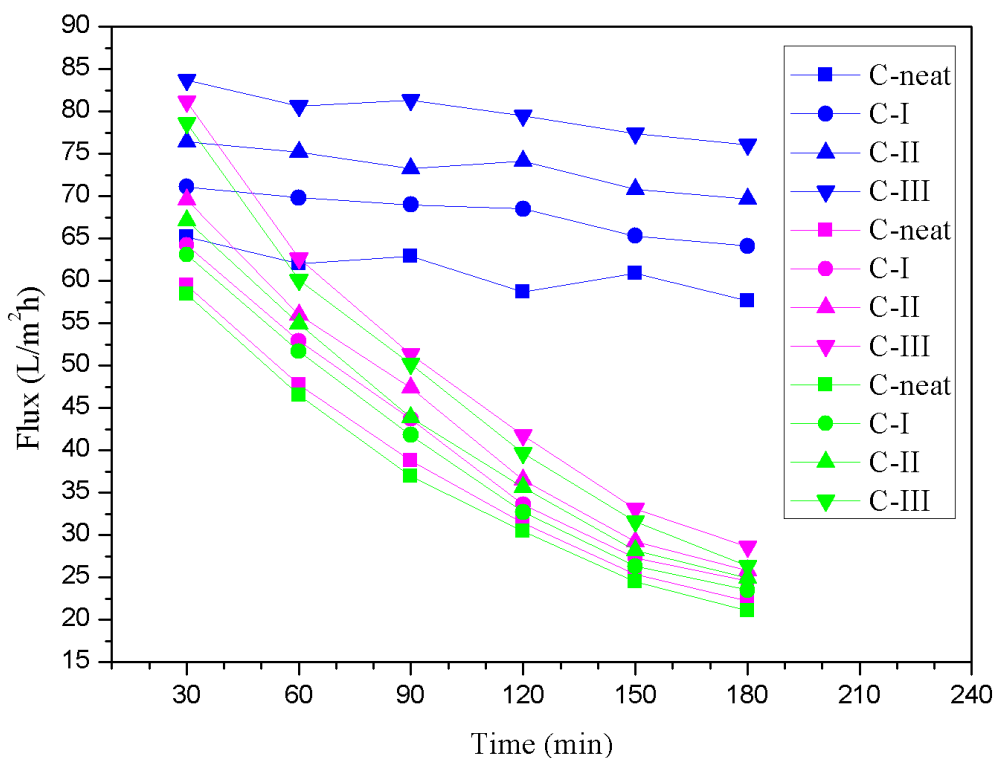
Membranes	Water contact angle	
	Top surface (°)	Bottom surface (°)
C-neat	69.2 ± 0.08 ^a	70.4 ± 0.05 ^a
C-I	62.4 ± 0.05 ^b	67.0 ± 0.04 ^b
C-II	55.4 ± 0.07 ^c	62.1 ± 0.06 ^c
C-III	51.3 ± 0.09 ^d	59.7 ± 0.08 ^d

421 ^{a-d}Values within the same column with various superscripts indicate significant differences ($p \leq 0.05$).

422

423 3.4. Membrane filtration performance

424 Fig. 6. shows flux changes of pure water, Co²⁺ solution, Ni²⁺ solution for different dual-layer membranes. As can
 425 be seen, the flux of pure water, Co²⁺ and Ni²⁺ solutions was found to increase with the increase in nanocellulose
 426 filler loading and this is going along with the rise in hydrophilicity as indicated by the reduction in the contact
 427 angle with more filler in the membranes. It was because the bigger nanocellulose amount could expose more polar
 428 hydroxyl groups (-OH) on the membrane surface, which thereby improved its reaction with water for high
 429 permeation (Daraei et al. 2016; Li et al. 2018). Moreover, the constantly increasing flux for both pure water and
 430 metal ion solutions throughout those nanocellulose filled membranes might prove that the good migration and
 431 dispersibility of nanocellulose particles on each dual-layer membrane surface (Karim et al. 2016; Liu et al. 2015).
 432 Theoretically, the decrease of average pore size from C-I (1.13 μm) to C-III (0.54 μm) membrane is suppose to
 433 reduce the permeability for solution penetration upon considering the membrane porous structure. However, the
 434 present membranes behaved conversely and the enhanced flux for the membranes in this work could be attributed
 435 to the compensation of improved porosity for the membrane from C-I (67%) to C-III (74%). Hence, the surface
 436 hydrophilicity, pore size and porosity played an important role in enhancing the permeation in the membrane (Ai
 437 et al. 2018; Xu et al. 2018).



439

440 **Fig. 6.** Flux changes of pure water (blue line), Co^{2+} solution (purple line), Ni^{2+} solution (green line) for dual-layer
 441 membranes with 0-3 wt% CNWs loadings.

442

443 The metal ions removal efficiency of the membranes was also examined by both batch and continuous modes of
 444 adsorptions and the obtained data are presented in Table 7. As can be observed, the C-II membrane showed the
 445 highest removal efficiency for Co^{2+} ions standing at 69% and 66% for Ni^{2+} ions in batch adsorption. On the other
 446 hand, the C-III showed the highest removal efficiency of 83% for Co^{2+} and 84% for Ni^{2+} ions under continuous
 447 adsorption mode. The smaller pore size in C-III membrane most likely prevented the metal ions accessibility to
 448 the internal anchoring sites during the test under batch adsorption mode. However, the presence of the pressure
 449 applied in the continuous operation could aid in improving the adsorption of internal contact area for metal ions
 450 in C-III due to the increased solutions penetration through the membrane (Fan et al. 2018; Liu et al. 2017).

451 For C-I membrane, it exhibited extremely lower metal ions removal in both batch and continuous adsorption
 452 modes when compared to C-II membrane though the C-I had relatively great surface wettability and porosity for
 453 high permeability. It might be attributed to the stronger size exclusion effect in C-II membrane reducing the
 454 penetration of metal ions and subsequently facilitated metal ions attachment on nanocellulose hydroxyl function
 455 sites via ion-dipole interactions. This phenomenon was in agreement with the adsorption result obtained in studies

456 reported in literature (Karim et al. 2016; Teow et al. 2018; Xu et al. 2018). In this work, the continuous adsorption
 457 mode was more efficient in removing metal ions than the batch adsorption mode. The estimated adsorption
 458 capacity of C-III membrane in continuous mode was the highest with 103.8 mg/g for Co^{2+} and 105.0 mg/g for
 459 Ni^{2+} , while the lowest adsorption with 41.3 mg/g of Co^{2+} and 38.8 mg/g of Ni^{2+} ions for C-neat membrane (Table
 460 7). The low adsorption capacity of C-neat membrane towards metal ions can be probably attributed to the
 461 intermolecular reaction with PLA polymer (Karim et al. 2016; Liu et al. 2016). Thus, it was confirmed that C-III
 462 membrane possessed the highest metal ions adsorption capacity. The obtained adsorption result was greater than
 463 the reported data by Liu et al. (2016) using TEMPO-oxidized cellulose nanofibers for removing Cu^{2+} ions with
 464 approximately 32 mg/g adsorption capacity. Meanwhile, this work also gave better adsorption values than data
 465 reported in Danso et al. (2018) in which 23.73 mg/g adsorption capacity of Zn^{2+} ions from metal coating
 466 wastewater and 10.50 mg/g adsorption capacity of Ba^{2+} ions from mining seep wastewater were observed using
 467 sulfur-ligand tethered cellulose nanofibers. Furthermore, the present results are comparable with those obtained
 468 by Liu et al. (2017) who produced carboxylated cellulose nanocrystal/polyethyleneimine composite membrane
 469 for Cr^{3+} ion removal showing about 50 mg/g adsorption capacity, while Teow et al. (2018) fabricated
 470 cellulose/gelatin composite hydrogel that showed 3 mg/g adsorption capacity of Cu^{2+} ions.

471

472 **Table 7.** Metal ions adsorption capacity and removal efficiency by dual-layer membranes with 0-3 wt% CNWs
 473 loadings.

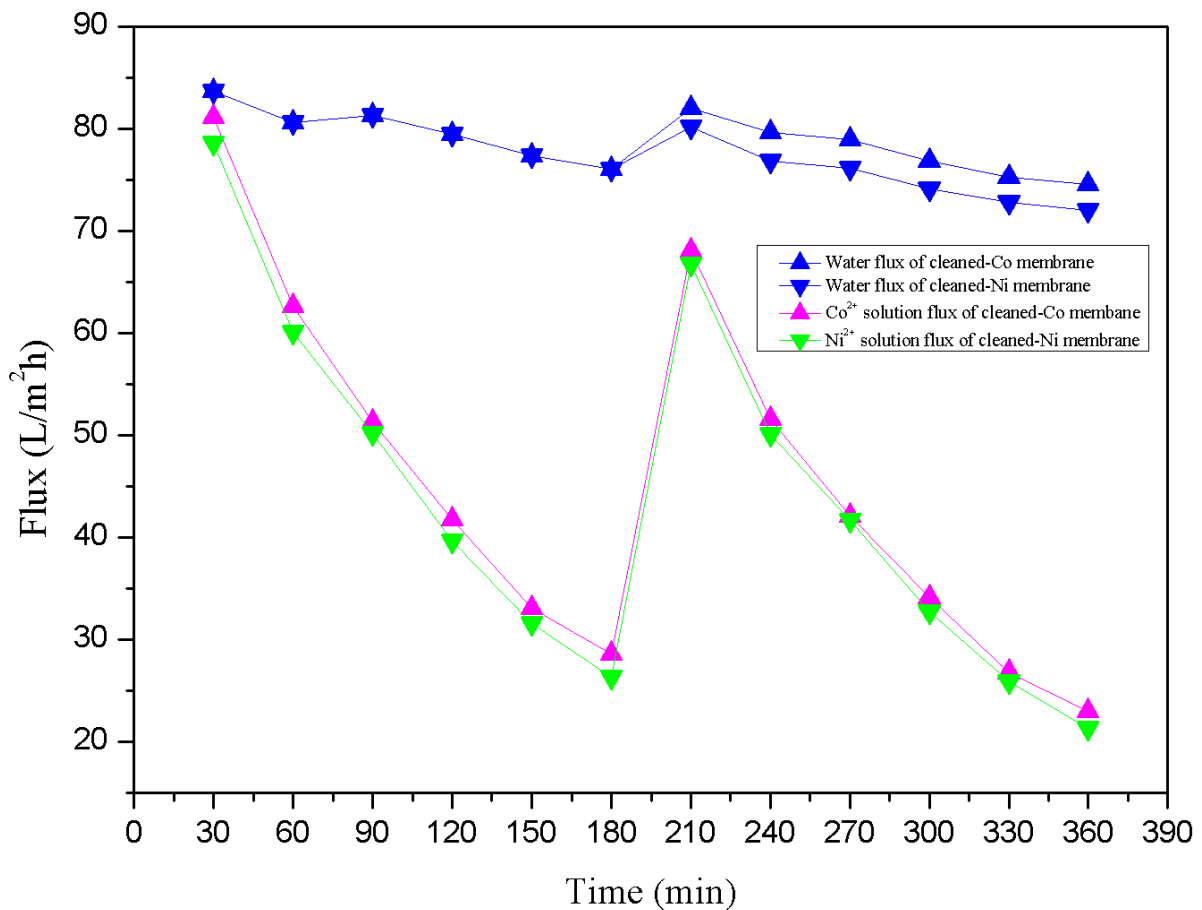
Membranes	Batch mode				Continuous mode			
	Adsorbed capacity (mg/g)		Removal efficiency (%)		Adsorbed capacity (mg/g)		Removal efficiency (%)	
	Co^{2+}	Ni^{2+}	Co^{2+}	Ni^{2+}	Co^{2+}	Ni^{2+}	Co^{2+}	Ni^{2+}
C-neat	32.5	35.0	26	28	41.3	38.8	33	31
C-I	48.8	47.5	39	38	52.5	51.3	42	41
C-II	86.3	82.5	69	66	93.8	96.3	75	77
C-III	78.8	77.5	63	62	103.8	105.0	83	84

474

475 Due to the great performance in metal ions removal, the C-III membrane was subjected to second cycle of filtration
 476 process to further study its anti-fouling property. As shown in Fig. 7, all cleaned-membranes for C-III showed
 477 sudden rise in flux between 180-210 min, attributing to the successfully removal of metal ions by deionized water
 478 during washing process prior to second filtration. However, the permeability fluxes in second filtration (210-360
 479 min) were reducing for both pure water and metal ion solutions when comparing to first filtration (30-180 min).
 480 This is owing to the blockage of pore channels by the remained metal clusters in the membrane (Liu et al. 2016;
 481 Teow et al. 2018). During adsorption, the sulfate function groups (SO_3^-) on nanocellulose acted as reducing agent

482 to synthesize Co and Ni elements from Co^{2+} and Ni^{2+} ions, which eventually aggregated to form metal
 483 microparticles (Karim et al. 2016). This was confirmed from FESEM images presented in Fig. 8 where Co (Fig.
 484 8a) and Ni (Fig. 8b) metal microparticles can be seen on the C-III membrane surface after adsorption process.
 485 However, the anti-fouling capability was considerably high with FR_w of 98% and 96%, while FR_p was 85% and
 486 84% for the cleaned-Co and cleaned-Ni membranes, respectively (Fig. 8). Interestingly, the membrane could still
 487 adsorb metal ions capacities in the second filtration cycle with values of 26.4 mg/g for Co^{2+} and 27.2 mg/g for
 488 Ni^{2+} ions. Therefore, these results provide further evidence confirming the great adsorption performance of C-III
 489 membrane signifying its strong potential for removal of heavy metal ions from wastewater treatment.

490

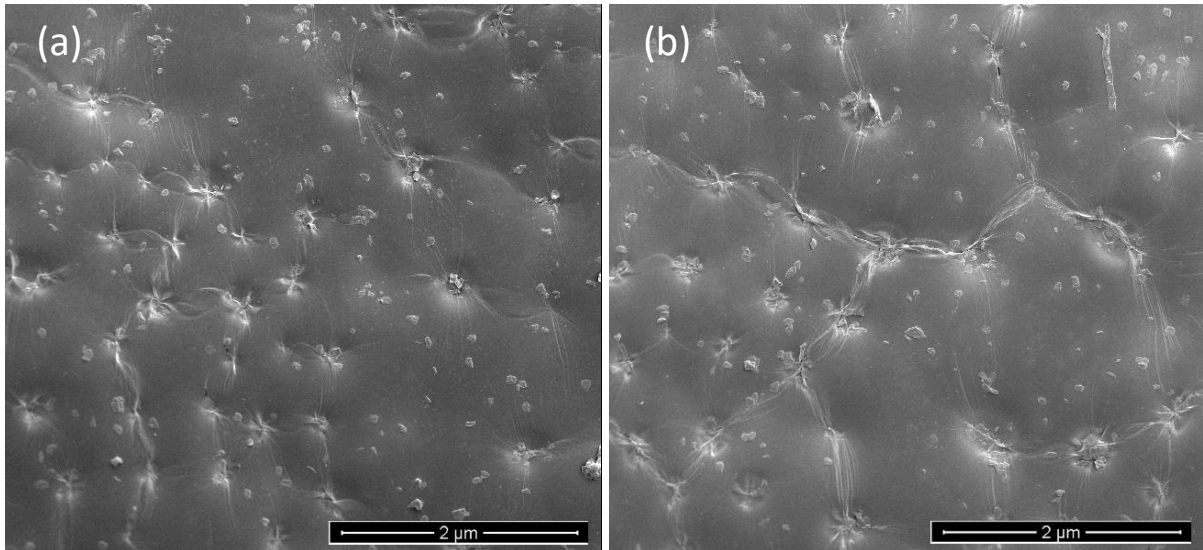


491

492

Fig. 7. Flux changes for C-III membrane in two filtration cycles.

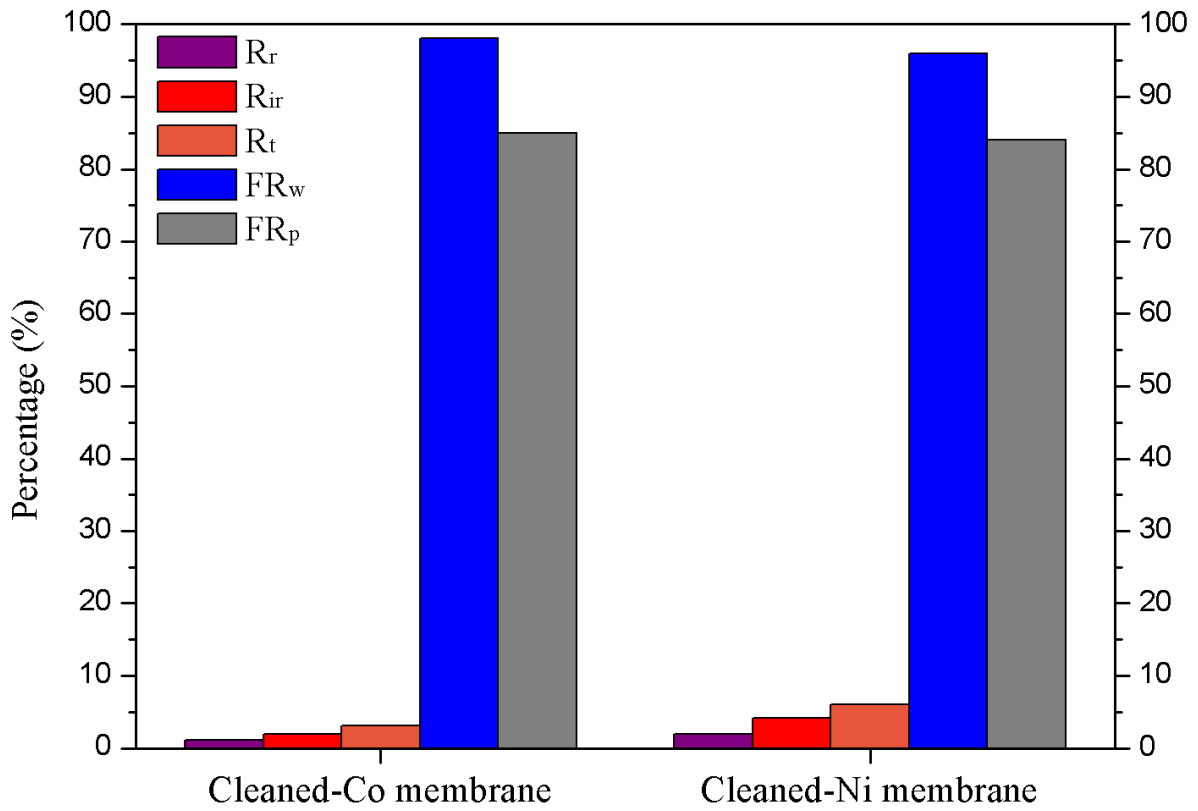
493



494

495 **Fig. 8.** FESEM images of C-III membrane with (a) Co and (b) Ni metal microparticles.

496



497

498 **Fig. 9.** Reversible fouling (R_r), irreversible fouling (R_{ir}), total fouling ratio (R_t), pure water flux recovery (FR_w)
 499 and metal ion solution flux recovery (FR_p) for C-III membrane.

500

501

502

503 3.5. Statistical analysis

504 The reproducibility of this work was studied with replicates data. From morphology, the BET replicates data
505 showed a prominent difference in the porosity and average pore size for each sample. Also, the insignificant
506 standard deviation values implied the ease of reproducing the membranes with similar porous structures (Table
507 2). In addition, the obtained tensile test replicates data presented the tensile strength and elongation at break were
508 significantly varying (at 95% confidence level) to each membrane sample. It was mainly affected by the complex
509 lamination adhesion between PLA and PBS polymeric layers. Furthermore, it was noticed the less significant
510 difference of Young's modulus in between C-neat and C-I, while also in between C-II and C-III membranes (Table
511 5). This indicated the nanocellulose loadings between 1 to 2 wt% are crucial for the interaction between
512 nanocellulose and polymers. Additionally, the standard deviation values were less than 0.1 for water contact
513 angles (Table 6), suggesting the presence of a good intereaction between membrane surface with polar groups
514 allowing water penetration and metal ions adsorption process.

515

516 4. Conclusion

517 Four types of CNWs filled PLA/PBS dual-layer membranes with different loadings was successfully prepared
518 using an integrated water vapor-induced and crystallization-induced phase inversions method. The new method
519 imparted a synergetic effect ~~on~~ to the polymer precipitation for both polymer layers and eventually boosted the
520 membrane filtration performance towards separation of heavy metal ions. The best performing membrane i.e., C-
521 III membrane showed tightly adhered polymeric layers, while maintaining high level of porosity and small pore
522 size compared to C-neat, C-I and C-II membranes. The C-I membrane exhibited the highest heat resistance
523 amongst all taking its low sulphated nanocellulose content into consideration. The temnsile properties were
524 enhanced for C-II and C-III membranes owing to the great interaction between the two polymer layers ~~in~~ providing
525 a good stress transferring property within the membranes' structures. The performance of wastewater filtration
526 showed that C-III membrane is very promising in removing metal ions such as Co^{2+} and Ni^{2+} and this is attributed
527 to its great water flux, high adsorption capacity, and anti-fouling property. Eventually, it can be concluded that
528 the newly adopted technique is a promising approach for sustainable preparation of nanocellulose-reinforced dual-
529 layer membranes having strong potential for application in removal of heavy metal ions from wastewater streams.

530

531 **Acknowledgements**

532 The author would like to acknowledge University Putra Malaysia (GP-IPS/2018/9626200) for financial support.

533 The authors are also grateful to Malaysian Industry-Government Group for High Technology (MIGHT) for

534 Financial support of this work Under Newton-Ungku Omar Fund Grant No: 6300873.

535

536 **Declaration**

537 We declare that there is no Animal studies or human participants involvement in the study, no

538 ethical clearance required.

539

540 **Conflicts of interest/Competing interests- No conflict of interest**

541

542 **References**

543 Ai J, Yang L, Liao G, Xia H, Xiao F (2018) Applications of graphene oxide blended poly(vinylidene fluoride)

544 membranes for the treatment of organic matters and its membrane fouling investigation. *Appl Surf Sci*

545 455:502-512. <https://doi.org/10.1016/j.apsusc.2018.05.162>

546 Arjmandi R, Hassan A, Haafiz MKM, Zakaria Z, Islam MS (2016) Effect of hydrolysed cellulose nanowhiskers

547 on properties of montmorillonite/polylactic acid nanocomposites. *Int J Biol Macromol* 82:998–1010.

548 <https://doi.org/10.1016/j.ijbiomac.2015.11.028>

549 Badawi NE, Ramadan AR, Esawi AMK, Morsi ME (2014) Novel carbon nanotube–cellulose acetate

550 nanocomposite membranes for water filtration applications. *Desalination* 344:79–85.

551 <https://doi.org/10.1016/j.desal.2014.03.005>

552 Bahremand AH, Mousavi SM, Ahmadpour A, Taherian M (2017) Biodegradable blend membranes of poly

553 (butylenesuccinate)/cellulose acetate/dextran: Preparation, characterization and performance. *Carbohydr*

554 *Polym* 173:497–507. <https://doi.org/10.1016/j.carbpol.2017.06.010>

555 Bai H, Zhou Y, Zhang L (2015) Morphology and mechanical properties of a new nanocrystalline cellulose/
556 polysulfone composite membrane. *Adv Polym Technol* 34(1). <https://doi.org/10.1002/adv.21471>

557 Bolisetty S, Peydayesh M, Mezzenga R (2019) Sustainable technologies for water purification from heavy metals:
558 review and analysis. *Chem Soc Rev* 48:463-487. <https://doi.org/10.1039/C8CS00493E>

559 Bonyadi S, Chung TS (2007) Flux enhancement in membrane distillation by fabrication of dual layer hydrophilic-
560 hydrophobic hollow fiber membranes. *J Membrane Sci* 306:134-146.
561 <https://doi.org/10.1016/j.memsci.2007.08.034>

562 Borkotoky SS, Dhar P, Katiyar V (2018) Biodegradable poly (lactic acid)/cellulose nanocrystals (CNCs)
563 composite microcellular foam: Effect of nanofillers on foam cellular morphology, thermal and wettability
564 behavior. *Int J Biol Macromol* 106:433-446. <https://doi.org/10.1016/j.ijbiomac.2017.08.036>

565 Cai Y, Guo J, Chen C, Yao C, Chung SM, Yao J, Lee IS, Kong X (2017) Silk fibroin membrane used for guided
566 bone tissue regeneration. *Mater Sci Eng C* 70(1):148-154. <https://doi.org/10.1016/j.msec.2016.08.070>

567 Chinyerenwa AC, Wang H, Zhang Q, Zhuang Y, Munna KH, Ying C, Yang H, Xu W (2018) Structure and thermal
568 properties of porous polylactic acid membranes prepared via phase inversion induced by hot water droplets.
569 *Polymers* 141:62-69. <https://doi.org/10.1016/j.polymer.2018.03.011>

570 Choi H, Yoon SH, Son M, Celik E, Park H, Choi H (2015) Efficacy of synthesis conditions on functionalized
571 carbon nanotube blended cellulose acetate membrane for desalination. *Desalin Water Treat* 57:7545-7554.
572 <https://doi.org/10.1080/19443994.2015.1025582>

573 Danso EA, Peraniemi S, Leiviska T, Bhatnagar A (2018) Synthesis of S-ligand tethered cellulose nanofibers for
574 efficient removal of Pb(II) and Cd(II) ions from synthetic and industrial wastewater. *Environ Pollut*
575 242:1988-1997. <https://doi.org/10.1016/j.envpol.2018.07.044>

576 Daraei P, Ghaemi N, Ghari HS, Norouzi M (2016) Mitigation of fouling of polyethersulfone membranes using an
577 aqueous suspension of cellulose nanocrystals as a nonsolvent. *Cellulose* 23:2025-2037.
578 <https://doi.org/10.1007/s10570-016-0937-7>

579 Fan T, Li Z, Cheng B, Li J (2018) Preparation, characterization of PPS micro-porous membranes and their
580 excellent performance in vacuum membrane distillation. *J Membrane Sci* 556:107-117.
581 <https://doi.org/10.1016/j.memsci.2018.03.084>

582 Fathizadeh M, Aroujalian A, Raisi A (2011) Effect of added NaX nano-zeolite into polyamide as a top thin layer
583 of membrane on water flux and salt rejection in a reverse osmosis process. *J Membrane Sci* 375:88–95.
584 <https://doi.org/10.1016/j.memsci.2011.03.017>

585 Galiano F, Briceño K, Marino T, Molino A, Christensen KV, Figoli A (2018) Advances in biopolymer-based
586 membrane preparation and applications. *J Membrane Sci* 564:562–586.
587 <https://doi.org/10.1016/j.memsci.2018.07.059>

588 Gao A, Liu F, Shi H, Xue L (2015) Controllable transition from finger-like pores to inter-connected pores of
589 PLLA membranes. *J Membrane Sci* 478:96–104. <https://doi.org/10.1016/j.memsci.2015.01.004>

590 Gokce O, Kasap M, Akpınar G, Ozkoc G (2017) Preparation, characterization, and in vitro evaluation of chicken
591 feather fiber-thermoplastic polyurethane composites. *J Appl Polym Sci* 134(45):1-9.
592 <https://doi.org/10.1002/app.45338>

593 Haafiz MKM, Hassan A, Khalil HPSA, Khan I, Inuwa IM, Islam MS, Hossain MS, Syakir MI, Fazita MRN (2015)
594 Bionanocomposite based on cellulose nanowhisker from oil palm biomass-filled poly(lactic acid). *Polym*
595 *Test* 48:133-139. <https://doi.org/10.1016/j.polymertesting.2015.10.003>

596 Hamad K, Kaseem M, Ayyoob M, Joo J, Deri F (2018) Polylactic acid blends: The future of green, light and
597 tough. *Prog Polym Sci* 85:83–127. <https://doi.org/10.1016/j.progpolymsci.2018.07.001>

598 Hossain KMZ, Felfel RM, Rudd CD, Thielemans W, Ahmed I (2014) The effect of cellulose nanowhiskers on the
599 flexural properties of self-reinforced polylactic acid composites. *React Funct Polym* 85:193–200.
600 <https://doi.org/10.1016/j.reactfunctpolym.2014.09.012>

601 Huang A, Peng X, Geng L, Zhang L, Huang K, Chen B, Gu Z, Kuang T (2018) Electrospun poly (butylene
602 succinate)/cellulose nanocrystals bionanocomposite scaffolds for tissue engineering: Preparation,
603 characterization and in vitro evaluation. *Polym Test* 71:101–109.
604 <https://doi.org/10.1016/j.polymertesting.2018.08.027>

605 Huang H, Qu X, Dong H, Zhang L, Chen H (2013) Role of NaA zeolites in the interfacial polymerization process
606 towards a polyamide nanocomposite reverse osmosis membrane. *RSC Adv* 3:8203–8207.
607 <https://doi.org/10.1039/C3RA40960K>

608 Kao ST, Teng MY, Li CL, Kuo CY, Hsieh CY, Tsai HA, Wang DM, Lee KR, Lai JY (2008) Fabricating PC/PAN
609 composite membranes by vapor-induced phase separation. *Desalination* 233:96–103.
610 <https://doi.org/10.1016/j.desal.2007.09.031>

611 Kargarzadeh H, Mariano M, Huang J, Lin N, Ahmad I, Dufresne A, Thomas S (2017) Recent developments on
612 nanocellulose reinforced polymer nanocomposites: a review. *Polymers* 132:368-393.
613 <https://doi.org/10.1016/j.polymer.2017.09.043>

614 Karim Z, Claudpierre S, Grahn M, Oksman K, Mathew AP (2016) Nanocellulose based functional membranes
615 for water cleaning: tailoring of mechanical properties, porosity and metal ion capture. *J Membrane Sci*
616 514:418-428. <https://doi.org/10.1016/j.memsci.2016.05.018>

617 Kiadeh SZH, Ghaee A, Mashak A, Mohammadnejad J (2017) Preparation of chitosan-silica/PCL composite
618 membrane as wound dressing with enhanced cell attachment. *Polym Adv Technol* 28(11):1396-1408.
619 <https://doi.org/10.1002/pat.4016>

620 Kian LK, Jawaid M, Ariffin H, Alothman OY (2017) Isolation and characterization of microcrystalline cellulose
621 from roselle fibers. *Int J Biol Macromol* 103:931–940. <https://doi.org/10.1016/j.ijbiomac.2017.05.135>

622 Kian LK, Jawaid M, Ariffin H, Thariq MTH, Karim Z (2019) Morphological, physico-chemical, and thermal
623 properties of cellulose nanowhiskers from roselle fibers. *Cellulose* 26:6599–6613.
624 <https://doi.org/10.1007/s10570-019-02543-5>

625 Li D, Yan Y, Wang H (2016) Recent advances in polymer and polymer composite membranes for reverse and
626 forward osmosis processes. *Prog Polym Sci* 61:104–155.
627 <https://doi.org/10.1016/j.progpolymsci.2016.03.003>

628 Li Y, Chung TS, Huang Z, Kulprathipanja S (2006) Dual-layer polyethersulfone (PES)/BTDA-TDI/MDI co-
629 polyimide (P84) hollow fiber membranes with a submicron PES-zeolite beta mixed matrix dense-selective
630 layer for gas separation. *J Membrane Sci* 277:28–37. <https://doi.org/10.1016/j.memsci.2005.10.008>

631 Li Y, Huang S, Zhou S, Fane AG, Zhang Y, Zhao S (2018) Enhancing water permeability and fouling resistance
632 of polyvinylidene fluoride membranes with carboxylated nanodiamonds. *J Membrane Sci* 556:154-163.
633 <https://doi.org/10.1016/j.memsci.2018.04.004>

634 Lin N, Chen Y, Hu F, Huang J (2015) Mechanical reinforcement of cellulose nanocrystals on biodegradable
635 microcellular foams with melt-compounding process. *Cellulose* 22:2629–2639.
636 <https://doi.org/10.1007/s10570-015-0684-1>

637 Liu C, Jin RN, Ouyang XK, Wang YG (2017) Adsorption behavior of carboxylated cellulose nanocrystal—
638 polyethyleneimine composite for removal of Cr(VI) ions. *Appl Surf Sci* 408:77–87.
639 <https://doi.org/10.1016/j.apsusc.2017.02.265>

640 Liu P, Oksman K, Mathew AP (2016) Surface adsorption and self-assembly of Cu(II) ions on TEMPO-oxidized
641 cellulose nanofibers in aqueous media. *J Colloid Interf Sci* 464:175–182.
642 <https://doi.org/10.1016/j.jcis.2015.11.033>

643 Liu TY, Li CK, Pang B, Bruggen BVD, Wang XL (2015) Fabrication of a duallayer (CA/PVDF) hollow fiber
644 membrane for RO concentrate treatment. *Desalination* 365:57–69.
645 <https://doi.org/10.1016/j.desal.2015.02.020>

646 Luzi F, Fortunati E, Jiménez A, Puglia D, Pezzolla D, Gigliotti G, Kenny JM, Chiralt A, Torre L (2016) Production
647 and characterization of PLA PBS biodegradable blends reinforced with cellulose nanocrystals extracted
648 from hemp fibres. *Ind Crops Prod* 93:276–289. <https://doi.org/10.1016/j.indcrop.2016.01.045>

649 Meng Y, Li A, Li H, Shen Z, Ma T, Liu J, Zhou Z, Feng Q, Sun Y (2020) Effect of membrane blocking on attached
650 cultivation of microalgae. *J Cleaner Prod* 124695. <https://doi.org/10.1016/j.jclepro.2020.124695>

651 Mi HY, Jing X, Peng J, Salick MR, Peng XF, Turng LS (2014) Poly(*ε*-caprolactone) (PCL)/cellulose nano-crystal
652 (CNC) nanocomposites and foams. *Cellulose* 21:2727–2741. <https://doi.org/10.1007/s10570-014-0327-y>

653 Minbu H, Ochiai A, Kawase T, Taniguchi M, Lloyd DR, Tanaka T (2015) Preparation of poly(L-lactic acid)
654 microfiltration membranes by a nonsolvent-induced phase separation method with the aid of surfactants. *J*
655 *Membrane Sci* 479:85–94. <https://doi.org/10.1016/j.memsci.2015.01.021>

656 Mizuno S, Maeda T, Kanemura C, Hotta A (2015) Biodegradability, reprocessability, and mechanical properties
657 of polybutylene succinate (PBS) photografted by hydrophilic or hydrophobic membranes. *Polym Degrad*
658 *Stability* 117:58-65. <https://doi.org/10.1016/j.polymdegradstab.2015.03.015>

659 Noorani S, Simonsen J, Atre S (2007) Nano-enabled microtechnology: polysulfone nanocomposites incorporating
660 cellulose nanocrystals. *Cellulose* 14:577–584. <https://doi.org/10.1007/s10570-007-9119-y>

661 Ojijo V, Malwela T, Ray SS, Sadiku R (2012) Unique isothermal crystallization phenomenon in the ternary blends
662 of biopolymers polylactide and poly[(butylene succinate)-co-adipate] and nano-clay. *Polymer* 53:505-518.
663 <https://doi.org/10.1016/j.polymer.2011.12.007>

664 Peng N, Widjojo N, Sukitpaneelit P, Teoh MM, Lipscomb GG, Chung TS, Lai JY (2012) Evolution of polymeric
665 hollow fibers as sustainable technologies: past, present, and future. *Prog Polym Sci* 37:1401–1424.
666 <https://doi.org/10.1016/j.progpolymsci.2012.01.001>

667 Perazzo A, Preziosi V, Guido S (2015) Phase inversion emulsification: current understanding and applications.
668 *Adv Colloid Interf Sci* 222:581-599. <https://doi.org/10.1016/j.cis.2015.01.001>

669 Phaechamud T, Chitrattha S (2016) Pore formation mechanism of porous poly(DL-lactic acid) matrix membrane.
670 *Mater Sci Eng C* 61:744–752. <https://doi.org/10.1016/j.msec.2016.01.014>

671 Pillay V, Dott C, Choonara YE, Tyagi C, Tomar L, Kumar P, du Toit LC, Ndesendo VMK (2013) A review of
672 the effect of processing variables on the fabrication of electrospun nanofibers for drug delivery applications.
673 *J Nanomater* 1-22. <https://doi.org/10.1155/2013/789289>

674 Planellas M, Sacristán M, Rey L, Olmo C, Aymamí J, Casas MT, Valle LJ, Franco L, Puiggalí J (2014) Micro-
675 molding with ultrasonic vibration energy: New method to disperse nanoclays in polymer matrices. *Ultrason*
676 *Sonochem* 21:1557–1569. <https://doi.org/10.1016/j.ultsonch.2013.12.027>

677 Qian S, Sheng K (2017) PLA toughened by bamboo cellulose nanowhiskers: Role of silane compatibilization on
678 the PLA bionanocomposite properties. *Compos Sci Technol* 148:59-69.
679 <https://doi.org/10.1016/j.compscitech.2017.05.020>

680 Sanjay MR, Madhu P, Jawaid M, Senthamaraiannan P, Senthil S, Pradeep S (2018) Characterization and
681 properties of natural fiber polymer composites: a comprehensive review. *J Cleaner Prod* 172:566-581.
682 <https://doi.org/10.1016/j.jclepro.2017.10.101>

683 Stoyanova N, Paneva D, Mincheva R, Toncheva A, Manolova N, Dubois P, Rashkov I (2014) Poly(L-lactide) and
684 poly(butylene succinate) immiscible blends: from electrospinning to biologically active materials. *Mater*
685 *Sci Eng C* 41:119–126. <https://doi.org/10.1016/j.msec.2014.04.043>

686 Sung SH, Chang Y, Han J (2017) Development of polylactic acid nanocomposite films reinforced with cellulose
687 nanocrystals derived from coffee silverskin. *Carbohydr Polym* 169:495–503.
688 <https://doi.org/10.1016/j.carbpol.2017.04.037>

689 Tanaka T, Nishimoto T, Tsukamoto K, Yoshida M, Kouya T, Taniguchi M, Lloyd DR (2012) Formation of depth
690 filter microfiltration membranes of poly(l-lactic acid) via phase separation. *J Membrane Sci* 396:101–109.
691 <https://doi.org/10.1016/j.memsci.2012.01.002>

692 Teow YH, Kam LM, Mohammad AW (2018) Synthesis of cellulose hydrogel for copper (II) ions adsorption. *J*
693 *Environ Chem Eng* 6:4588–4597. <https://doi.org/10.1016/j.jece.2018.07.010>

694 Tijink MS, Wester M, Sun J, Saris A, Bolhuis-Versteeg LA, Saiful S, Joles JA, Borneman Z, Wessling M,
695 Stamatialis DF (2012) Stamatialis, A novel approach for blood purification: mixed-matrix membranes
696 combining diffusion and adsorption in one step. *Acta Biomater* 8:2279–2287.
697 <https://doi.org/10.1016/j.actbio.2012.03.008>

698 Waqas S, RoilBilad M, Man ZB, Suleman H, Nordin NAH, Jaafar J, Othman MHD, Elma M (2020) An energy-
699 efficient membrane rotating biological contactor for wastewater treatment. *J Cleaner Prod* 124544.
700 <https://doi.org/10.1016/j.jclepro.2020.124544>

701 Xia QC, Liu ML, Cao XL, Wang Y, Xing W, Sun SP (2018) Structure design and applications of dual-layer
702 polymeric membranes. *J Membrane Sci* 562:85–111. <https://doi.org/10.1016/j.memsci.2018.05.033>

703 Xiong Z, Zhong Y, Lin H, Liu F, Li T, Li J (2017) PDLA/PLLA ultrafiltration membrane with excellent
704 permeability, rejection and fouling resistance via stereocomplexation. *J Membrane Sci* 533:103–111.
705 <https://doi.org/10.1016/j.memsci.2017.03.028>

706 Xu Y, Li Z, Su K, Fan T, Cao L (2018) Mussel-inspired modification of PPS membrane to separate and remove
707 the dyes from the wastewater. *Chem Eng J* 341:371–382. <https://doi.org/10.1016/j.cej.2018.02.048>

708 Zhang X, Wang X (2018) Polybutylene succinate/cellulose nanocrystals: Role of phthalic anhydride in squeeze
709 oriented bionanocomposites. *Carbohydr Polym* 196:254–261.
710 <https://doi.org/10.1016/j.carbpol.2018.04.124>

- 711 Zhao Y, Li M, Yuan Z, Li X, Zhang H, Vankelecom IFJ (2016) Advanced charged sponge-like membrane with
712 ultrahigh stability and selectivity for vanadium flow batteries. *Adv Funct Mater* 26(2):210-218.
713 <https://doi.org/10.1002/adfm.201503390>
- 714 Zhong L, Ding Z, Li B, Zhang L (2012) Preparation and characterization of polysulfone/sulfonated
715 polysulfone/cellulose nanofibers ternary blend membranes. *Bioresources* 10(2):2936–2948.
716 <https://doi.org/10.15376/biores.10.2.2936-2948>.
- 717 Zuo J, Chung TS, O'Brien, GS, Kosar W (2017) Hydrophobic/hydrophilic PVDF/Ultem (R) dual-layer hollow
718 fiber membranes with enhanced mechanical properties for vacuum membrane distillation. *J Membrane Sci*
719 523:103–110. <http://doi.org/10.1016/j.memsci.2016.09.030>

Figures

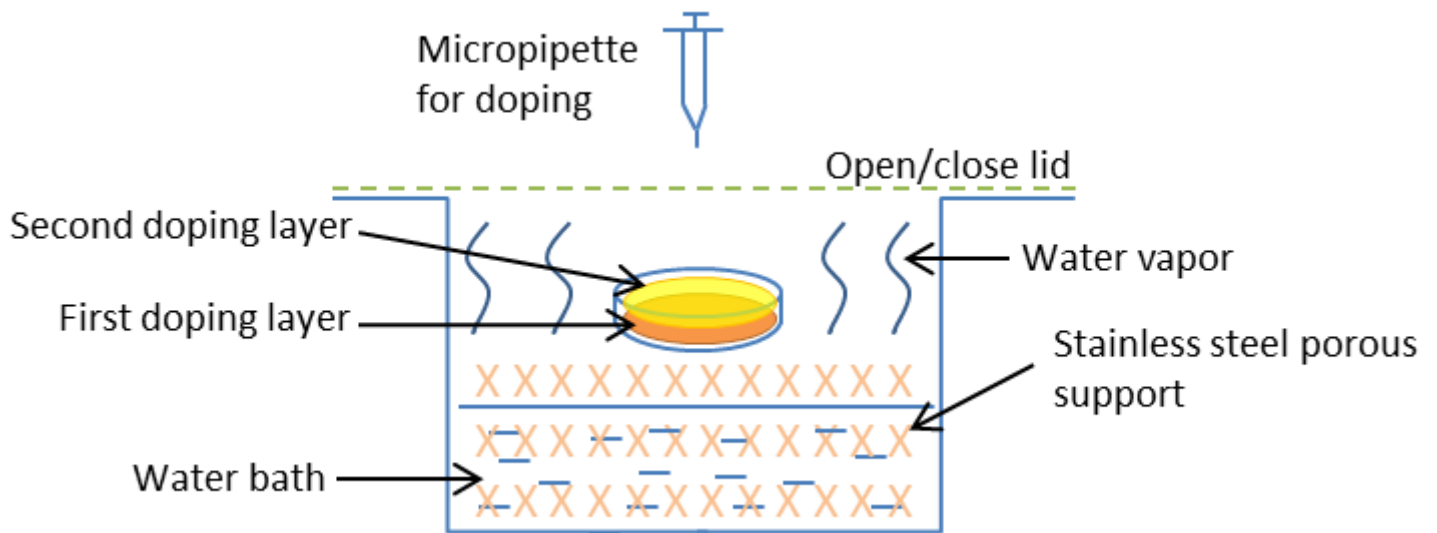


Figure 1

Schematic diagram of experimental phase inversion process for dual layer membrane precipitation.

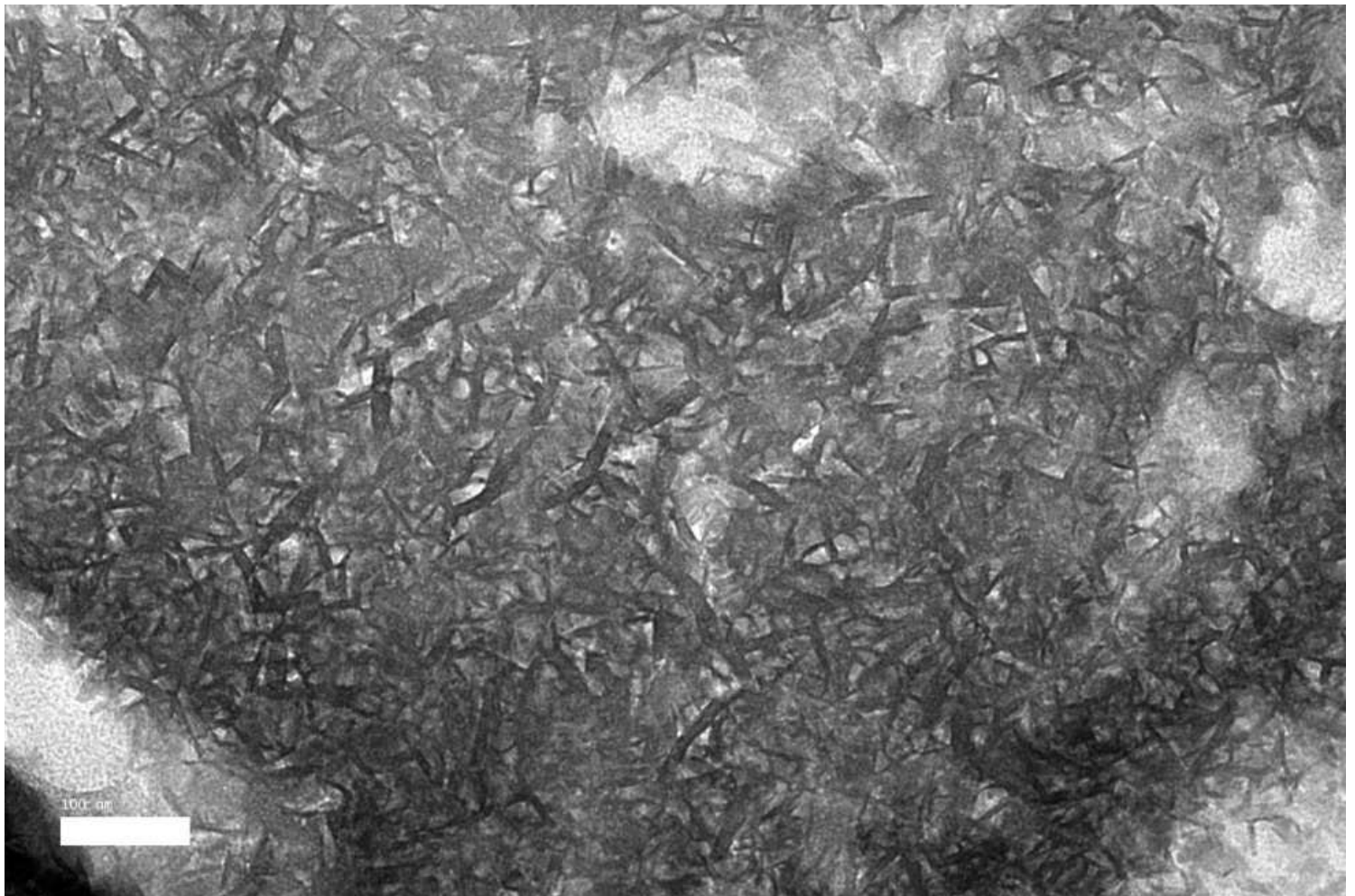


Figure 2

TEM image of formed CNW.

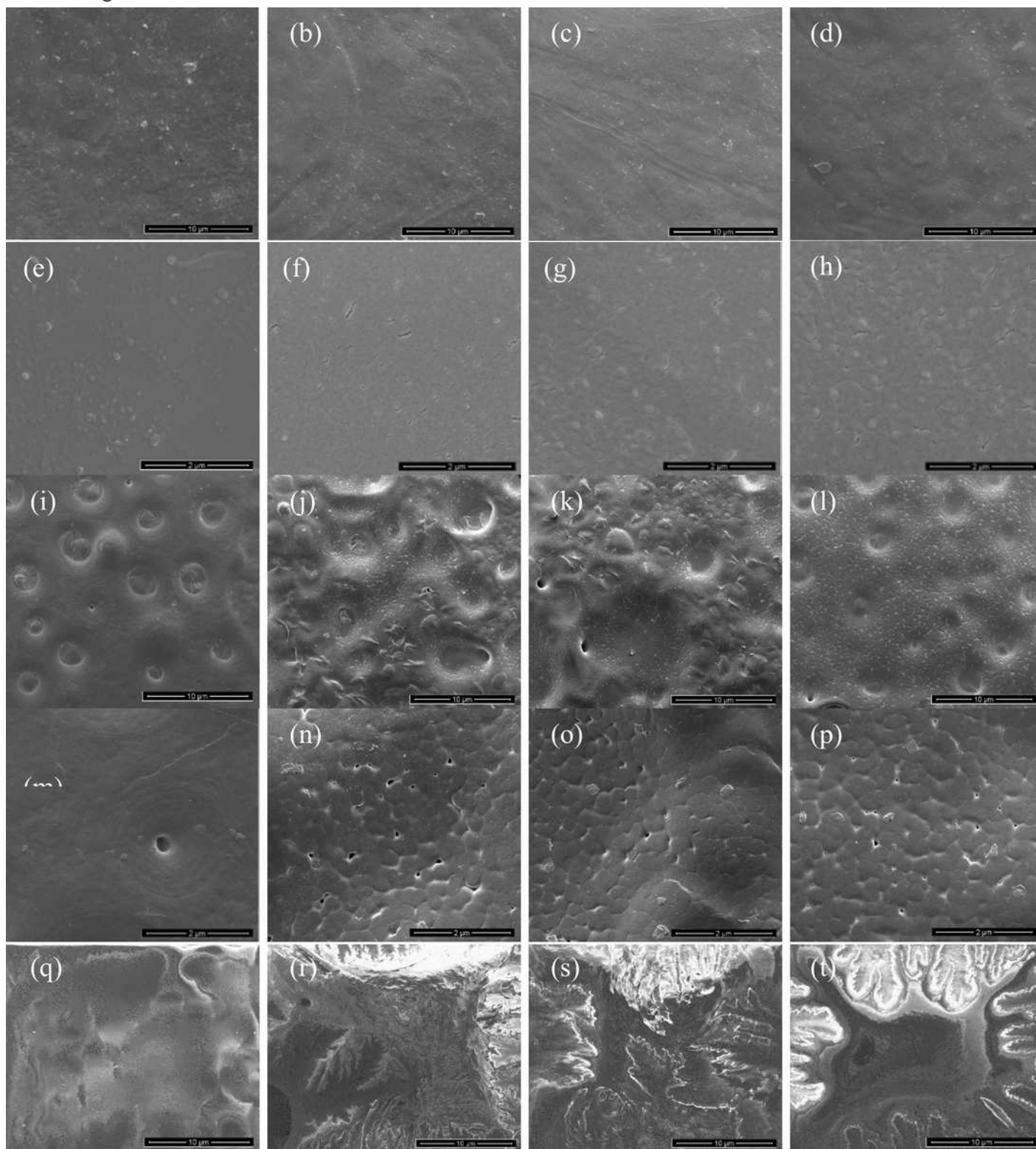


Figure 3

FESEM images of C-neat (a, e, i, m, q), C-I (b, f, j, n, r), C-II (c, g, k, o, s), and C-III (d, h, l, p, t) membranes for top-surface at 10000 x (a-d) and 50000 x (e-h) magnifications; bottom-surface at 10000 x (i-l) and 50000 x (m-p) magnifications; cross-sectional view at 10000 x (q-t) magnification morphology.

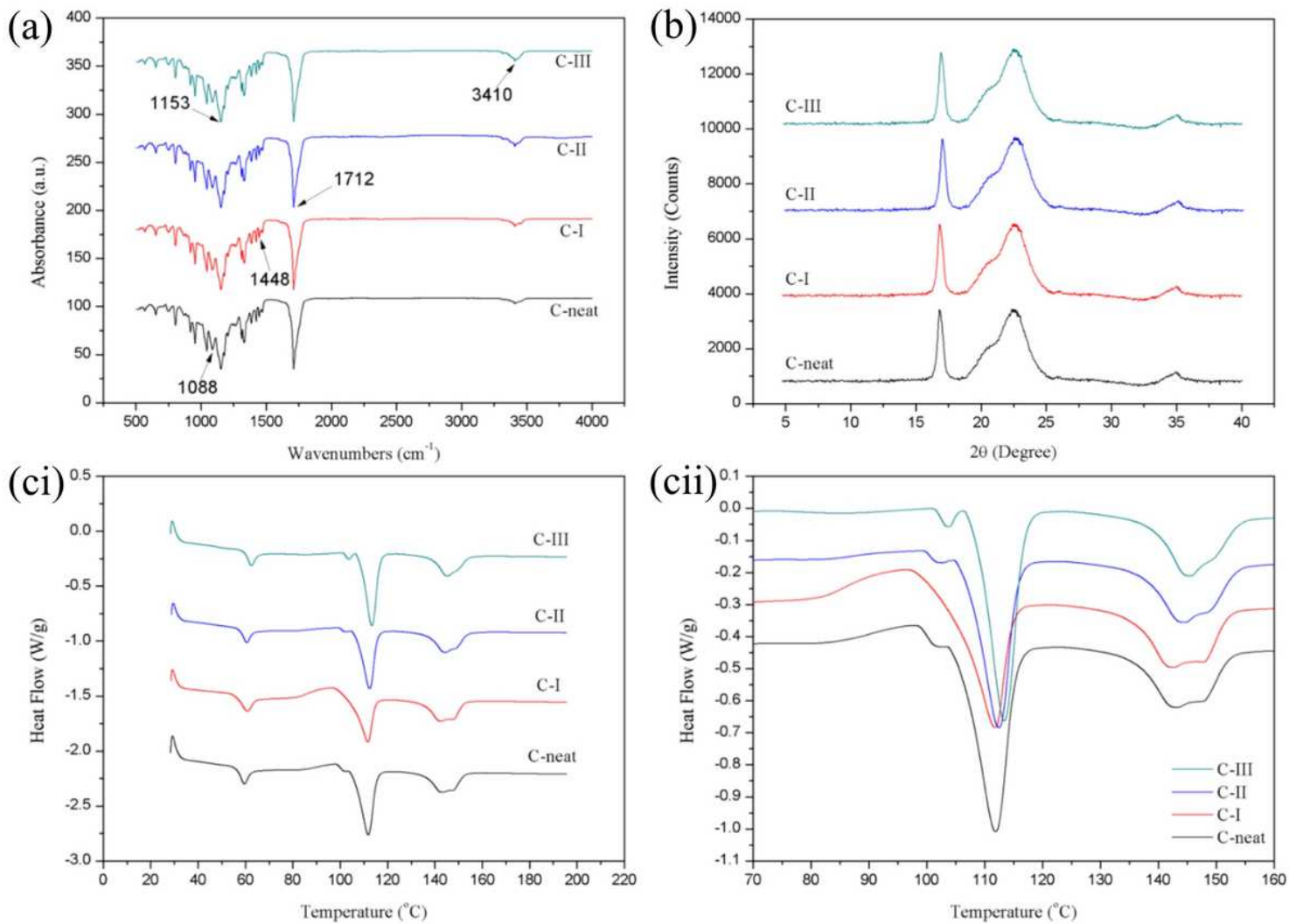


Figure 4

Various changes in properties of dual-layer membranes observed in: (a) FTIR spectra (b) XRD diffractograms and (ci and cii) full and zoomed DSC curves, respectively.

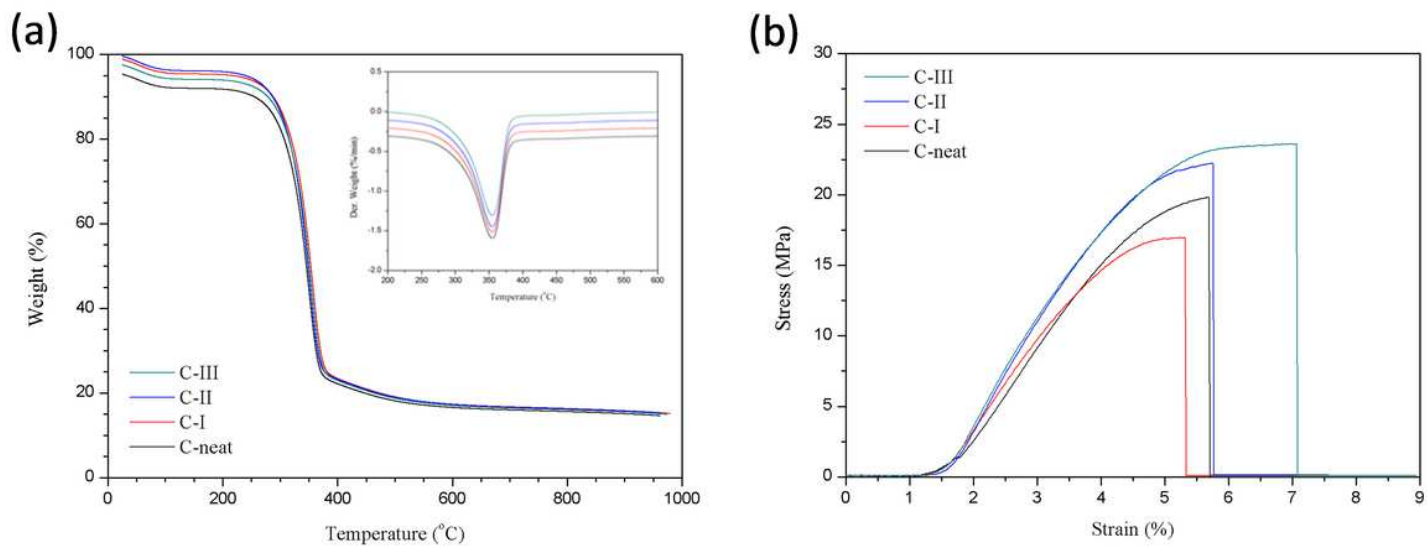


Figure 5

(a) TGA curves (with plotted DTG curves) and (b) mechanical stress-strain curves of dual-layer membranes.

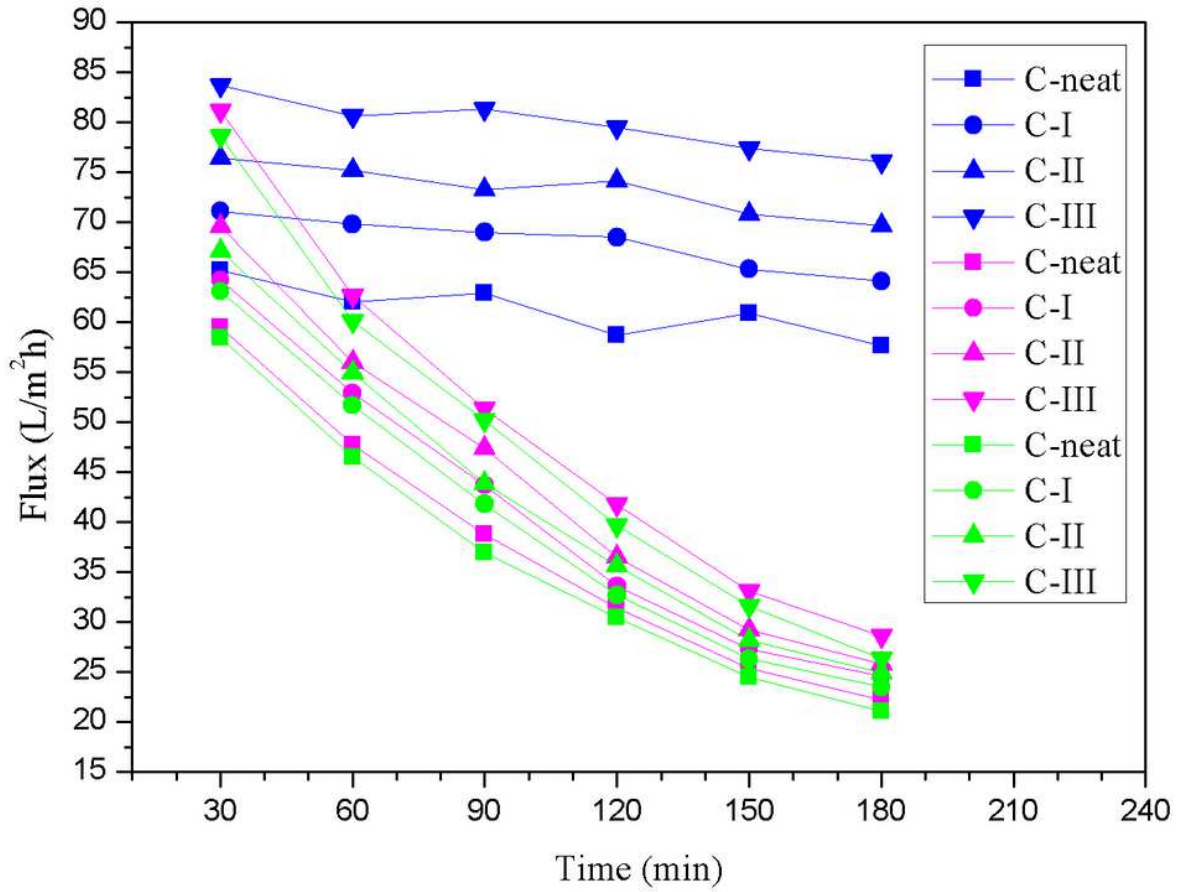


Figure 6

Flux changes of pure water (blue line), Co²⁺ solution (purple line), Ni²⁺ solution (green line) for dual-layer membranes with 0-3 wt% CNWs loadings.

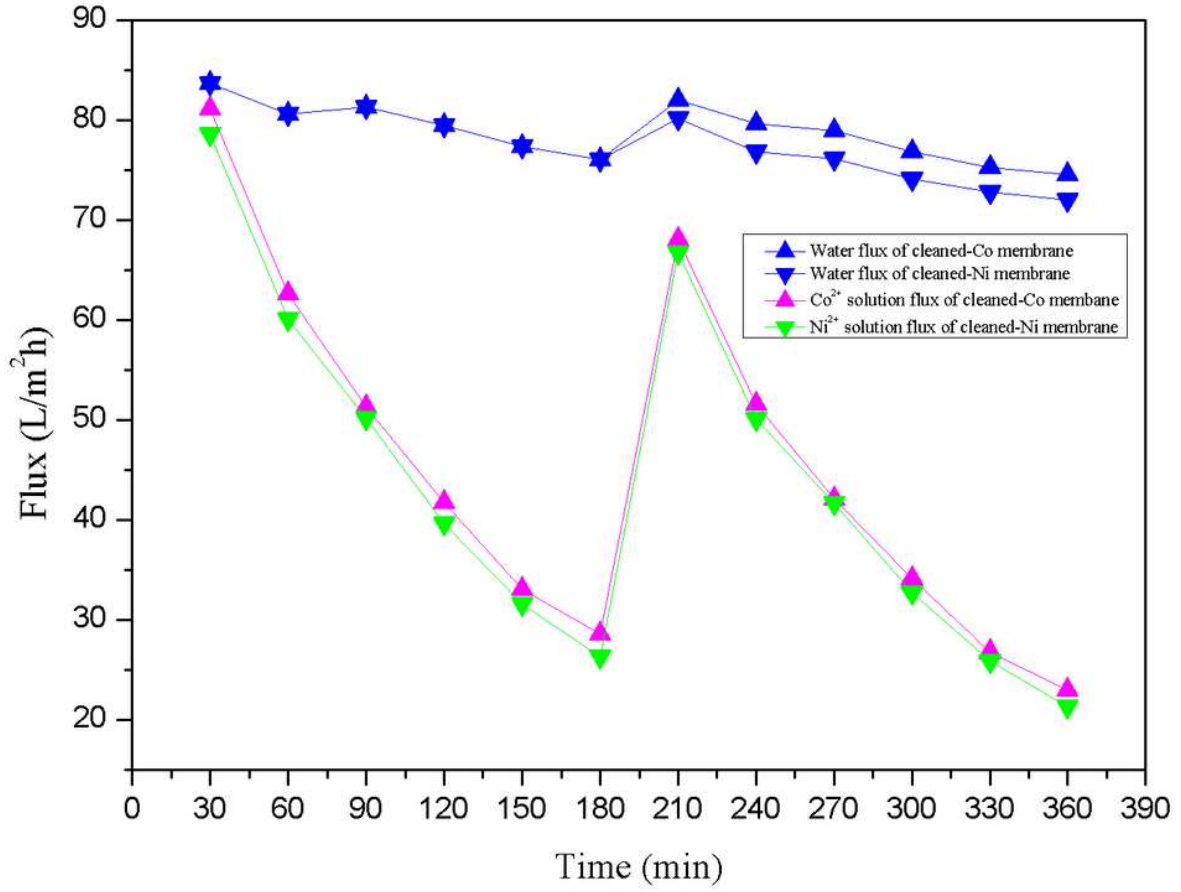


Figure 7

Flux changes for C-III membrane in two filtration cycles.

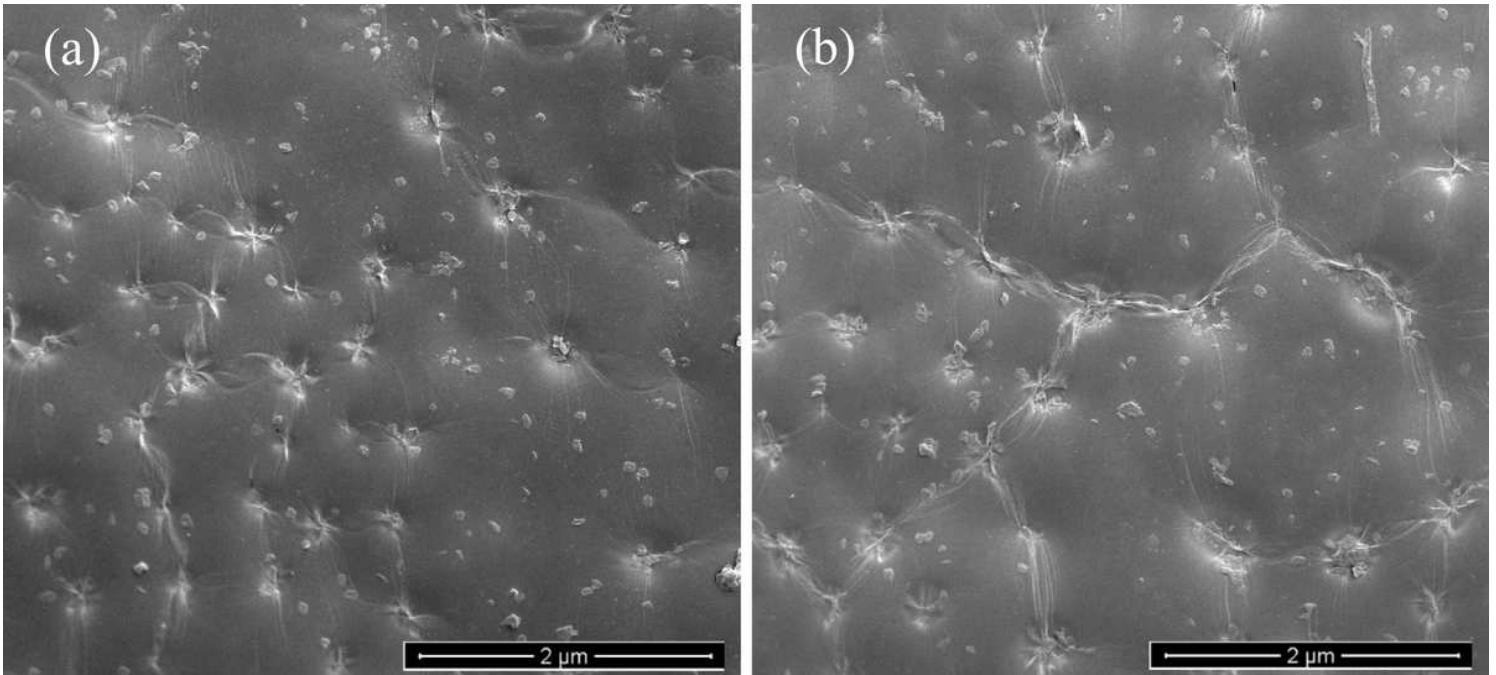


Figure 8

FESEM images of C-III membrane with (a) Co and (b) Ni metal microparticles.

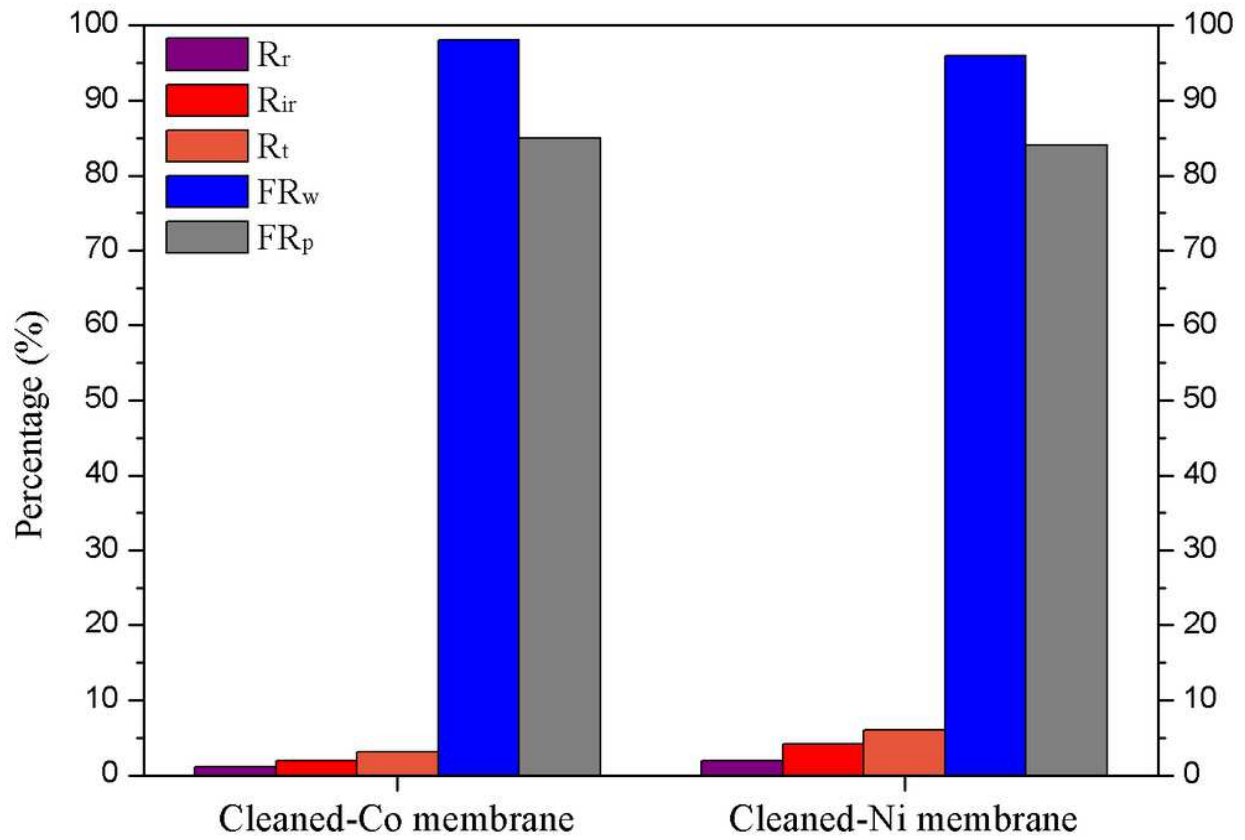


Figure 9

Reversible fouling (R_r), irreversible fouling (R_{ir}), total fouling ratio (R_t), pure water flux recovery (FR_w) and metal ion solution flux recovery (FR_p) for C-III membrane.